# A NUMERICAL STUDY OF NEAR-FIELD DISPERSION WITHIN AND ABOVE A FOREST CANOPY

By

STEVEN LEE EDBURG

A thesis submitted in partial fulfillment of
the requirements for the degree of

MASTER OF SCIENCE in MECHANICAL ENGINEERING

WASHINGTON STATE UNIVERSITY
School of Mechanical and Materials Engineering

AUGUST 2005

To the Faculty of Washington State University:

The members of the Committee appointed to examine the thesis of STEVEN LEE EDBURG find it satisfactory and recommend that it be accepted.

_____
Chair

_____

_____

## ACKNOWLEDGEMENTS

This research project was funded by a cooperative with the United States Department of Agriculture (U.S.D.A.) Forest Service. I thank my committee members, Drs David Stock, Brian Lamb, and Prashanta Dutta for their guidance throughout this research project. I thank Dr. Harold Thistle for providing the opportunity to conduct this research.

I thank Michael Shook for his support with computer resources, Gene Allwine and Wes Throop for field data, and Julia Flaherty for Fluent support.

Lastly, I thank my parents Stan and Judy Edburg and my sister and brother AnnMarie and Jeff for all their love and support.

**A Numerical Study of Near-Field Dispersion within and above a Forest Canopy.**

## ABSTRACT

by Steven Lee Edburg, M.S.
Washington State University
August 2005

The motivation for this project was to develop a tool to guide forest managers in protecting high value forest stands from bark beetle infestations. Several field experiments have been conducted in multiple forest canopies linking tracer gas concentration fields with meteorological and canopy parameters. Field experiments are often limited by cost, locations, and meteorological conditions. Numerical simulations are far less expensive and allow for many variations in flow parameters such as atmospheric stability, wind speed and direction.

Near-field pheromone dispersion within and above a southern loblolly pine canopy with neutral and unstable atmospheric conditions was investigated using large eddy simulation (LES). LES captures coherent structures within and above the canopy which are responsible for the majority of scalar transport into and out of forest canopies. LES resolves large energy containing eddies while modeling smaller dissipative eddies using a sub grid scale model. The model incorporates canopy effects based on leaf area index (LAI), leaf area density (LAD), and stem density. Convective conditions are also modeled using a heat source term based on above canopy heat flux. Results of the LES are compared with experimental data from a recent tracer gas field study. The LES

solution predicts higher mean velocity and concentration within the canopy, but demonstrates similar instantaneous trends for velocity and concentration.

## TABLE OF CONTENTS

## LIST OF FIGURES

## LIST OF TABLES

## NOMENCLATURE

| | |
|---|---|
| $a$ | Extinction coefficient |
| $a_p$ | Linearized coefficient |
| $a_{nb}$ | Linearized coffiecent |
| $A_T$ | Area of a single trunk ($m^2$) |
| $C_2$ | Inertial loss coefficient (1/m) |
| $C_d$ | Leaf drag coefficient |
| $C_{d_T}$ | Cylinder drag coefficient |
| $C_s$ | Smagorinsky coefficient |
| $C_p$ | Specific heat of air (J/kg – K) |
| $d$ | Distance from the wall (m) |
| $D_i$ | Mass diffusion coefficient ($m^2$/s) |
| $F$ | Cumulative leaf area index |
| $h$ | Canopy height (m) |
| $H$ | Height of the domain (m) |
| $L$ | Length of the domain (m) |
| $L_s$ | Mixing length scale (m) |
| $L_h$ | Length scale at canopy height (m) |
| $L_u$ | Stream-wise length scale (m) |
| $L_w$ | Vertical length scale (m) |
| $Qn$ | Heat flux ($W/m^2$) |
| $S_h$ | Heat source ($W/m^3$) |
| $S_i$ | Momentum sink ($n/m^3$) |
| $\bar{S}_{ij}$ | Resolved scale rate of strain (1/s) |
| $t^+$ | Non-dimensional time |
| $u_h$ | Wind speed at canopy height (m/s) |
| $u_i$ | Velocity (m/s) |
| $u_i'$ | Fluctuating velocity component (m/s) |
| $u_*$ | Friction velocity (m/s) |
| $u^+$ | Non-dimensional velocity |
| $V$ | Cell volume ($m^3$) |
| $W$ | Width of the domain (m) |
| $y^+$ | Non-dimensional wall coordinate |
| $Y_i$ | Species mass fraction |

## Greek Letters

| | |
|---|---|
| $\alpha$ | Thermal diffusivity ($m^2/s$) |
| $\alpha_z$ | Leaf area density ($m^2/m^3$) |
| $\beta$ | Thremal expansion coefficient (1/K) |
| $\delta_{ij}$ | Kroneker delta |
| $\theta$ | Potential temperature |
| $\kappa$ | von Kármán constant |
| $k$ | Thermal conductivity ($W/m^2$-K) |
| $\mu$ | Dynamic viscosity (Pa-s) |
| $\mu_t$ | Sub-grid turbulent viscosity (kg/m-s) |
| $\nu$ | Kinematic viscosity ($m^2/s$) |
| $\rho$ | Density ($kg/m^3$) |
| $\tau_{ij}$ | Sub-grid stress tensor (Pa) |
| $\phi$ | Scalar variable |
| $\overline{\phi}$ | Filtered scalar variable |

# CHAPTER 1: INTRODUCTION

## 1.1. Motivation and Objectives

The motivation for this research was to develop a tool to guide forest managers in protecting high value forest stands from bark beetle infestations. Protecting forest stands from insect damage has been a priority of the U.S.D.A. Forest Service for many years, and will remain a priority for the foreseeable future. The Western Pine Beetle (*Dendroctonus brevicomis*) (WPB), Mountain Pine Beetle (*Dendroctonus ponderosae*) (MPB), and the Southern Pine Beetle *(Dendroctonus frontalis Zimmermann*) (SPB), are members of a group of beetles known as bark beetles. Bark beetles use a complex pheromone communication system to control their population in host trees by emitting aggregation and anti-aggregation pheromones. Aggregation pheromones are emitted by the bark beetle to attract mates to a host tree. Anti-aggregation pheromones are emitted to prevent overpopulation of a host tree and promote the attack of other trees in the stand (Thistle, Peterson et al. 2004).

Bark beetle infestations have dramatically increased over the past several years due to ecological factors including drought, tree stand age, and forest canopy density. This has directly impacted recreational use, wildlife habitat, and silvicultural practice. The U.S.D.A Forest Service reported a 70 percent reduction of the red-cockaded woodpecker habitat in the Daniel Boone National Forest located in southern Kentucky in a 2003 America's Forest Health Update (U.S.D.A. Forest Service 2003). They also reported that 34,000 acres of lodgepole pine in Colorado are at moderate to high risk of MPB infestation.

Many techniques have been used by the U.S.D.A Forest Service to prevent damage to forest stands and control bark beetle infestations. Control strategies can be divided into destructive and non-destructive methods. Slash and burn, and cut and leave are examples of destructive control strategies and are used primarily after an infestation has occurred to prevent further stand damage. For high value forest stands, such as national parks or wildlife habitat refugees, destructive control strategies are not widely used. One popular non-destructive control strategy is using synthetic pheromones. Aggregation pheromones are used to attract insects to traps, and anti-aggregation pheromones are used to repel insects from an area. A popular anti-aggregation control strategy for the bark beetle is to hang permeable packets containing synthetic anti-aggregation pheromones in the forest stand. The specific spacing or pattern for placement of packets is usually determined by the forest manager on site. However, there is little quantitative information available on pheromone transport and dispersion within forest canopies to guide the forest manager in optimal spacing of pheromone packets (Thistle, Peterson et al. 2004). Dilution rates of pheromones as a function of canopy type and density, atmospheric stability, and terrain would be useful to forest managers to guide them in optimal placement of pheromone packets.

Surrogate pheromone dispersion studies have been developed and conducted by a multi-organizational team over the past several years. Led by the U.S.D.A. Forest Service, these field studies were conducted in different canopy types and densities, under varying atmospheric conditions, and in different geographic locations. These studies have provided a base for the scientific understanding of pheromone dispersion within forest canopies. Experiments are irreplaceable, and have been the forefront in providing

scientific understanding of atmospheric processes; however, field experiments of this magnitude have several drawbacks: they are expensive and complex, the experimentalist has no control over atmospheric conditions, and data collected on site is usually processed after the experiment is concluded. Numerical studies are often used to complement experimental studies, and have several advantages over field experiments.

Numerical studies can complement experimental studies by allowing the modeler complete control over atmospheric conditions. Furthermore, computations are far less expensive than field campaigns. However numerical studies require initial conditions that must be specified by the modeler. Careful attention must be paid to the initial and boundary conditions for realistic numerical simulations. There are many numerical models that can be used to simulate atmospheric dispersion. One must clearly define the processes that govern the phenomena to be study, and make the appropriate choice for a numerical model.

Scalar transport within and above plant canopies has been studied by a number of experimentalists and numerical modelers. Raupach and Thom (1981), and Finnigan (2000) have provided reviews of plant canopy turbulence measurements and numerical studies. From the experimental and numerical studies they determined that scalar transport into and out of plant canopies is governed by large scale, intermittent, organized motion that is correlated in space and time. These correlated organized structures are defined as coherent structures. Coherent structures can only be captured if the experimentalist has fast response instruments, and similarly, if the modeler uses a numerical approach that captures the instantaneous velocities and concentrations. Large

Eddy Simulation (LES) is able to capture the dynamics of atmosphere-plant canopy interactions, including the important coherent structures.

LES explicitly solves the governing equations of fluid motion (Navier-Stokes equations) for the large scales of turbulence. Smaller scales of turbulence are parameterized using a sub-grid scale model. LES is very computationally expensive compared to Gaussian plume based models, but capturing the dynamics of atmosphere-plant canopy interactions with a numerical model, such as LES, can provided valuable insight into the plant canopy turbulence phenomena (Shaw and Schumann 1992; Su, Shaw et al. 1998; Patton, Davis et al. 2001; Patton, Sullivan et al. 2003). LES is not a "push button model", and will not be used directly by a forest manager in the foreseeable future; however LES can be used to gain insight into the phenomena governing pheromone dispersion within forest canopies, and can be used to develop simpler models.

A field experiment, when coupled with numerical models, is the best method for understanding pheromone dispersion within forest canopies. The objective of this research is to investigate the use of LES for simulating pheromone dispersion within and above forest canopies.

# CHAPTER 2: BACKGROUND

## 2.1. Atmospheric Flows

### 2.1.1. Atmosphere-Plant Canopy Flows

The atmosphere is comprised of many layers, each layer occupying a finite section of the atmosphere. The atmospheric boundary layer (ABL) is located from the surface up to a maximum height of several kilometers. The lowest level of the ABL that interacts with canopies is called the surface layer. The interaction between air masses in the surface layer and plant canopies has been studied for many years. As with most progress to date in turbulent flows, the knowledge acquired in interactions between plant canopies and the surface layer was pioneered by experimentalists. Field and wind tunnel experiments have provided a base of knowledge on atmosphere-plant canopy interactions.

Raupach, Finnigan et al. (1996) presented a set of 'family portraits' of statistical wind and turbulence profiles taken from measurements conducted by in canopies varying from wheat canopies to forest canopies. Canopy height (h), roughness density (λ), mean velocity at canopy height ($\overline{u}_h = \overline{u}(h)$), and friction velocity at the canopy height ($\overline{u}_* = \sqrt{-\overline{u'w'}}$) are used as non-dimensionalizing parameters. The family portraits include mean velocity profiles, vertical Reynolds stress, standard deviation of velocity, correlation coefficients, skewness, length scales, and leaf area densities for each canopy type. These figures provide insight into canopy flow in a wide range of canopies. Some of the main points concluded by Finnigan (2000) regarding the flow structure in plant canopies are:

i. An inflection point in the velocity profile exists at the top of the canopy (h). The inflection point plays a critical role in canopy turbulence and transport.

ii. A maximum shear region exists at the canopy height (h), with strength described by a length scale $L_h = \left(\overline{u}(h)/(\partial \overline{u}(h)/\partial z\right)$.

iii. Above the canopy height (h), the standard logarithmic mean velocity profile is observed. Within the canopy an exponential mean velocity profile is roughly observed.

iv. A constant stress region exists just above the canopy height (h).

v. The vertical Reynolds stress, ($-\overline{u'w'}$), rapidly decays within the canopy which suggesting momentum is absorbed within the canopy.

vi. Standard deviations are scattered, however, an indication of 'sloshing' motion within the canopy is observed.

vii. Turbulence around the top of the canopy transports much more momentum and scalars than what is observed in the surface layer.

viii. Length scales are large, on the order of the canopy height ($L_u = h$) in the stream-wise direction, and ($L_w = h/3$) in the vertical direction.

The differences in the flow from the canopy height h to 3h are so profound that this region is called the 'roughness sub-layer' by Raupach, Antonia et al. (1991). Furthermore, Finnigan (2000) differentiated the region occupied by vegetation, the 'canopy layer' (0 – h), and the roughness sub-layer (h - 3h). In the surface layer, eddy diffusivities are often used to parameterize turbulent motion. Gaussian models take advantage of these parameterizations to provide concentration distributions as functions of downstream distance. However these parameterizations are invalid in the canopy layer

due to negative and zero gradients (Denmead and Bradley 1987). Negative or zero gradients inside the canopy leads one to believe other mechanisms are at work.

Coherent structures were discovered in turbulent boundary layers by experimentalists using flow visualization (Kline, Reynolds et al. 1967) and fast response instruments (Wallace, H. Eckelmann et al. 1972; Willmarth and Lu 1972). Until these findings it was believed that turbulence consisted of random motion. Two types of coherent structures that are prevalent in flows over rough surfaces are bursts and sweeps. A burst is defined as low velocity fluid slowly rising away from the wall, and a sweep is defined as high velocity fluid rapidly moving towards the wall (Bernard and Wallace 2002).

One technique used to detect coherent structures with fast response instruments is quadrant analysis. In quadrant analysis the velocity signal is first decomposed into stream-wise ($u'$) and vertical ($v'$) fluctuating velocity components by subtracting the mean velocity from the instantaneous velocities. The sign of $u'$ and $v'$ at one instant determines where the point is plotted: Q1 ($u' > 0,\ v' > 0$); Q2 ($u' < 0,\ v' > 0$); Q3 ($u' < 0,\ v' < 0$); Q4 ($u' > 0,\ v' < 0$) (Wallace, H. Eckelmann et al. 1972; Willmarth and Lu 1972). High speed sweeps are found in quadrant Q4, and low speed bursts are found in quadrant Q2. These findings showed that bursts and sweeps dominate the turbulent motion close to the wall. Some of the first experimental work on coherent structures within forest canopies were by Baldocchi and Meyers (1988a); Amiro (1990); and Gardiner (1994), who used two point correlations to find the length scales in the canopy were $L_u = h$, and $L_w = h/3$. Finnigan (1979) used quadrant analysis to study a wheat crop, and Baldocchi and Meyers (1988b) applied the technique to forest canopies. Quadrant

analysis provided insight into specific properties of coherent structures above and within a canopy. Many experimentalists have observed that sweeps are responsible for 50% of the stress inside a canopy while only occurring over 10% of the time (Finnigan 2000).

Spectral analysis is another analysis tool made available by the advent of fast response instruments and allows one to look at the energy spectrum from a turbulence signal (Kaimal and Finnigan 1994). Kolomgorov's energy cascade theory is a well known description of turbulence spectra which states that energy flows from high levels to low levels, each cascading to the next. However, this theory does not allow for backscatter or short circuiting of energy. Finnigan (2000) defines 'short circuiting' as large scales being rapidly broken up into small scales by the foliage, thus transferring energy directly from the large scales to the small scales. This short circuiting leads to the notion that the foliage has a net dissipative effect on the turbulence. That is, large energy containing scales are rapidly converted into smaller dissipative scales, which remove energy from the system.

The foliage in a plant canopy is comprised of elements with a wide range of scales. That is, a forest canopy is composed of small scales (needles) up to large scales (trunks). To understand how this wide range of scales affects the turbulence structure one can look at the turbulent kinetic energy (TKE) budget. TKE is produced at the canopy height (h) and just below the canopy height (h) by the strong shear layer at the canopy height (h). TKE is dissipated by the foliage by three paths. First, by pressure drag on the canopy elements. Secondly, by large scales losing energy to heat generated by viscous drag. And finally, by transferring TKE to the inertial sub-range by the traditional energy cascade.

2.1.2. Atmospheric Stability

Atmospheric stability is a measure of the vertical motion in the ABL, and has a direct influence on the turbulence (e.g. mixing) intensity in the ABL. Three conditions, neutral, stable, and convective, are often used to describe the stability of the atmosphere. Neutral, stable, and convective conditions can occur over the same geographic location at different time periods. The potential temperature ($\theta$) profile can be used to determine which stability regime is present. A neutral stability condition is present if the vertical motion of an air parcel is not affected by the local potential temperature ($\frac{\partial \theta}{\partial z} = 0$), where z is the vertical distance above the surface. Stable conditions are present when the vertical motions of an air parcel are suppressed ($\frac{\partial \theta}{\partial z} > 0$), and convective conditions are present when the vertical motions of an air parcel are enhanced ($\frac{\partial \theta}{\partial z} < 0$) (Seinfeld and Pandis 1998).

Atmospheric stability has a direct influence on pheromone dispersion. During stable conditions, turbulence is suppressed and dispersion is at a minimum. Stable conditions are unfavorable for dispersion, and cause high concentration plumes to travel long distances. In convective conditions, turbulence is enhanced, causing mixing and entrainment of air within a plume. This leads to low plume concentrations, furthermore, convective conditions enhance the magnitude of bursts and sweeps. Plume dispersion is not affected by local potential temperature in neutral conditions. The height above the ground where the production of turbulence by mechanical forces equals the production of turbulence by buoyancy forces is the Monin Obukhov length (Seinfeld and Pandis 1998).

This length scale is used to describe the stability in the atmosphere and has been applied to determine the stability in canopy flow simulations (Leclerc, Beissner et al. 1990).

## 2.2. Bark Beetles

### 2.2.1. Species of Interest

The Western Pine Beetle (*Dendroctonus brevicomis*) (WPB), Mountain Pine Beetle (*Dendroctonus ponderosae*) (MPB), and the Southern Pine Beetle *(Dendroctonus frontalis Zimmermann*) (SPB), are bark beetles that are commonly found in the U. S. Pheromone dispersion field experiments have been conducted by the U.S.D.A. Forest Service around the U.S. for the past several years in oak-hickory, lodgepole pine, loblolly pine, and ponderosa pine canopies located in Montana, Oregon, and Louisiana. Each region is habitat for one species of bark beetle. The numerical study presented here will be used to compliment the Louisiana field experiment, where the SPB is the species of interest.

### 2.2.2. Life Cycle

Bark beetles are a parasite to trees and spend most of their life cycle as larva under the bark of a host tree. A pioneer beetle finds a host tree and releases an aggregation pheromone to attract mates to a tree. Potential mates will respond to the aggregation pheromone in large numbers. The beetles will mate and lay larva in the bark of the host tree. Larva will live off the host tree until the next emergence, and then repeat the cycle by emerging and locating a host tree. A sufficient number of larva feeding from a host tree can kill it.

### 2.2.3. Pheromone Communication

Bark beetles use a very complex pheromone communication system to control the population of a host tree and promote the attack of other trees in the stand (Thistle, Peterson et al. 2004). Once a host tree is located, the beetle will release an aggregation pheromone to attract potential mates to mating grounds. Different pheromones are released by male and female beetles at different concentrations. Aggregation pheromones are released in high doses until a target or overpopulation is achieved in the host tree. It is at this point where the host tree's defenses are overcome, and an anti-aggregation pheromone is released to prevent further population of the host tree and promote the attack of other trees in the stand.

### 2.2.4. Control Strategies

The U.S.D.A. Forest service has a number of control strategies in place that have a varying degree of success. Depending on the infestation location and detection time of the infestation destructive control strategies may be implemented. Destructive control strategies are often the most effective control strategy if an infestation has already occurred. An example of a destructive control strategy is the 'slash and burn' method. In this method the effective trees are cut and piled inside the stand and burned. This method eliminates host trees and therefore the beetles in them. Destructive methods are not feasible in high value forest stands such as national parks or wildlife refugees. In these cases a forest manager may turn to a non-destructive management strategy.

An example of a non destructive management strategy is the use of synthetic pheromones to either attract or repel beetles from a high risk area. These methods can be used prior to, or in defense of an infestation. Aggregation pheromones are used in

conjunction with traps to attract and trap beetles in a given area, while anti-aggregation pheromones are used to repel beetles from a high risk area. Anti-aggregation pheromones have been used for pest control for many years with limited and varying success.

When dispersing an anti-aggregation pheromone within a canopy for pest control, the forest manager is faced with the challenge of determining optimal packet spacing. There is very little quantitative information available for forest managers to guide them in the placement of these anti-aggregation pheromones. From field experiments, it was shown that the dilution rates of pheromones within forest canopies have a dependence on meteorological parameters, forest canopy parameters, and terrain features (Thistle, Peterson et al. 2004). Thus, the forest manage should include variation in packet placement to suit local conditions.

## 2.3. Experimental Studies

### 2.3.1. Experimental Design

Recent field studies have provided insight into pheromone dispersion within forest canopies (Thistle, Peterson et al. 2004). Four canopies were studied: two ponderosa pine canopies, an oak hickory canopy, and a lodgepole pine canopy. The same experimental design was used for each canopy type. On each test day sulfur hexafluoride ($SF_6$), tracer gas was released at a steady rate from a point source locate 1.5 m above the canopy ground. Each study involved 4.5 hour tests on nine separate days. Start times were varied to cover a range of conditions during the campaign.

An array of syringe samplers was deployed on 5m, 10m, and 30m radius circles centered at the $SF_6$ release. These samplers collected thirty minute average samples for analysis of tracer gas concentrations. A real time $SF_6$ analyzer was used to measure instantaneous $SF_6$ concentrations at one point in the canopy.

Three-axis, 15 cm pathlength, sonic anemometers were used to gather meteorological data; one positioned at the source, and three others on a tower at heights of 2.5 m, 15 m and 25.2 m above ground level. The sampling frequency was set at 10 Hz for each sonic anemometer. Canopy height was nominally 15 m. Two levels of 1min averaged wind speed and direction, humidity, temperature, and net radiation were also collected using two 7 m high meteorological towers. One sided leaf area index (LAI) was measured at each site. A SODAR was deployed off site in Louisiana, measuring vertical profiles of wind direction and wind speed from 20 m to 600 m at equidistant levels each 20 m apart. Further details can be found in Thistle et al (2004).

2.3.2. Case Study

The focus of this numerical study is to compliment the Louisiana data set collected in Winnfield, LA on May 15$^{th}$ 2004 through May 26$^{th}$ 2004. This particular field study was chosen because more extensive measurements were collected, and a vertical $SF_6$ sampler was deployed along with a SODAR. Both of these instruments were not used in the other field experiments. Another unique aspect about the Louisiana field experiment is the canopy was thinned in four stages and tracer gas tests were conducted for each stage. It is thought that canopy thinning influences the pheromone dispersion and thus has a direct impact on reducing the risk of forest stands to bark beetle infestations.

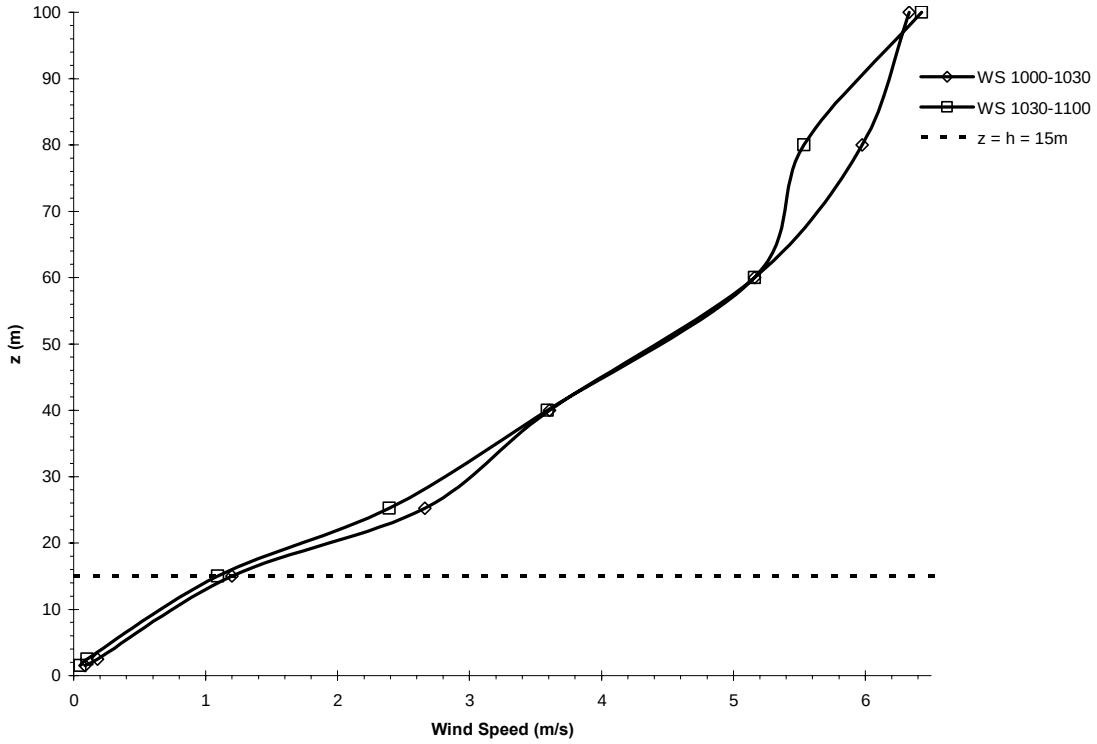


**Figure 1: 30min average wind speed on May 25th 2005 from 1000-1030 and 1030-1100 (Winnfield, LA).**

A specific test period occurring on May 25th at 1000-1100 was selected to evaluate the model. This period represents the final thinning, in which the LAI was approximately 2.0. Figure 1 shows wind speed as a function of height from the sonic anemometers and the SODAR, while Figure 2 shows the corresponding wind direction. Thirty minute averaged $SF_6$ concentration on the five meter arc is shown in Figure 3, the intersection of the grid lines represents the release point and the radius of the circle is proportional to the concentration. The 30 min average concentration does not suggest there is prevailing winds within the canopy, rather the air parcels are 'sloshing' around in all directions. Figure 4 supports the notion of this 'sloshing' of the plume, where the continuous $SF_6$ analyzer shows hits and misses of the $SF_6$ plume over five minutes.

Data from this case study will be revisited in Chapter 5, where the model will be evaluated for this time period.

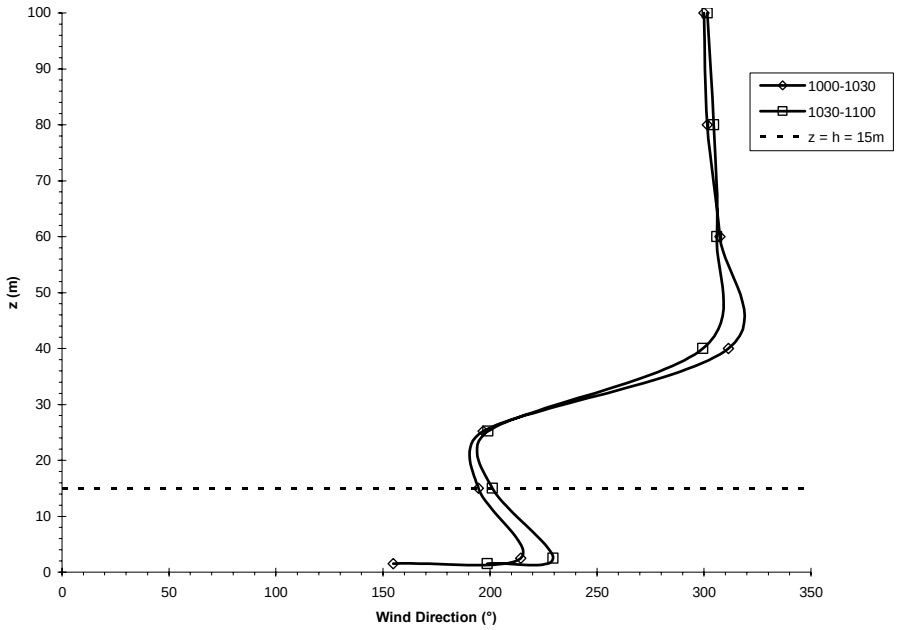


**Figure 2: 30min average wind direction on May 25th 2005 from 1000-1030 and 1030-1100 (Winnfield, LA).**

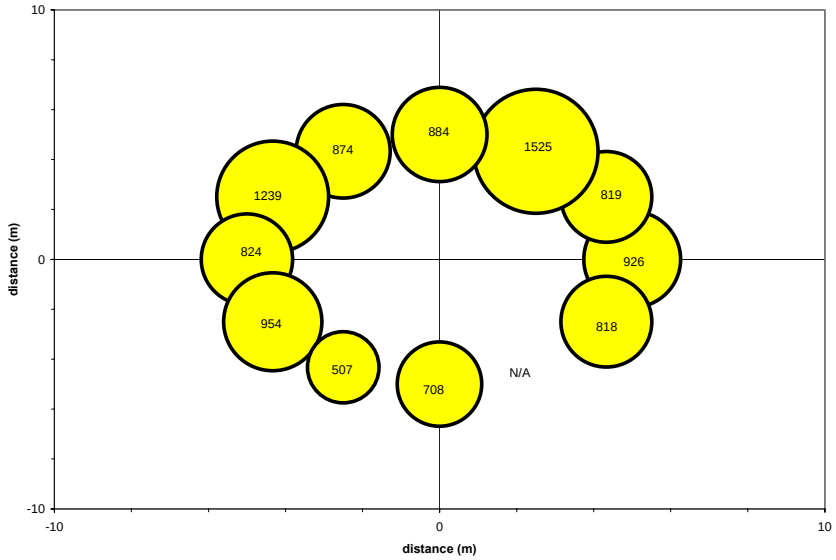


**Figure 3: 30 minute average $SF_6$ concentration from syringe samplers located on the 5m arc on May 25th 2005 between 1000 and 1030 (Winnfield, LA). Note: Concentration of $SF_6$ in ppt is listed inside each circle which corresponds to one sampler, distance is measured from release point.**

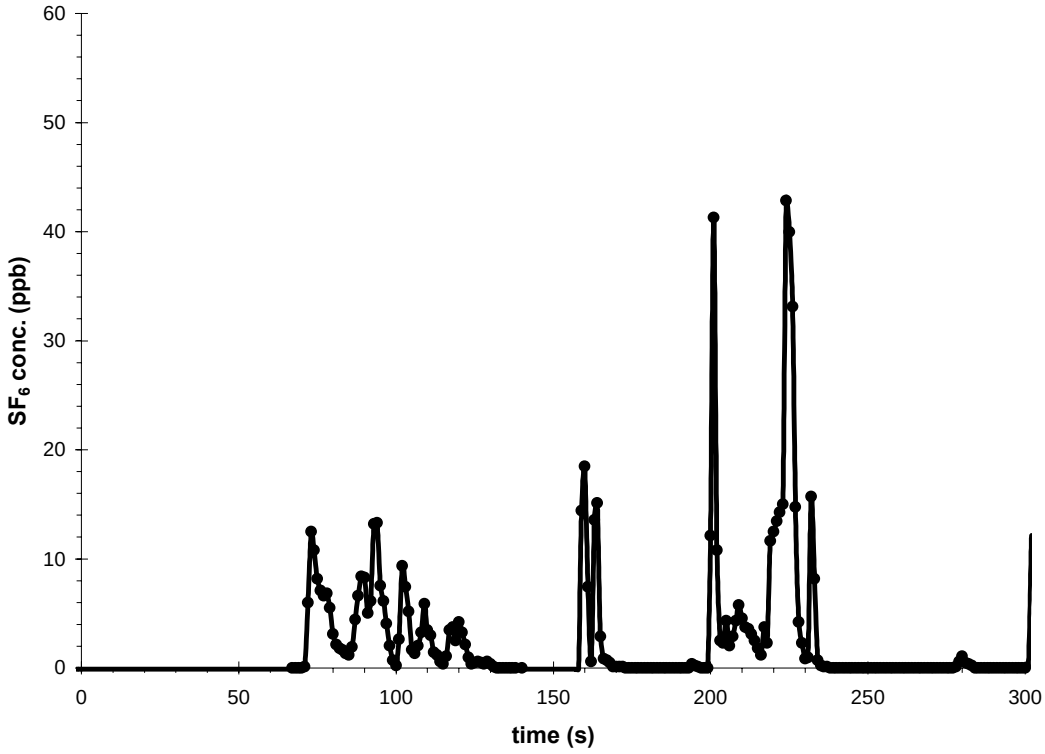


**Figure 4: $SF_6$ concentration (ppb) from a continuous analyzer located 10m from the release on May 25th 2005.**

## 2.4. Numerical Modeling Approach

The numerical modeling approach presented consists of three main parts: a preprocessor, a solver, and a postprocessor. Generation of a finite computational domain, comprised of finite computational elements or volumes, around complex geometries is performed with the preprocessor. The modeled governing equations are approximated into a set of algebraic equations and solved over the finite domain with the solver. Finally, a postprocessor is used to display and manipulate the solved data set with two and three dimensional plots, vectors, contours, animations, etc.

The Navier-Stokes equations are non-linear partial differential equations that describe the fluid flow of a Newtonian fluid and have analytical solutions only for a few

special cases, such as laminar flow in a pipe or channel. One must turn to numerical methods to solve these equations for complex engineering applications.

Three main approaches used to numerically solve the Navier-Stokes equations are Direct Numerical Simulation (DNS), Large Eddy Simulation (LES), and Reynolds Averaged Navier Stokes (RANS). DNS is a numerical solution approach that explicitly solves the Navier Stokes equations over all of the scales of motion (large and small). By solving the equations over all of the scales the complete dynamics of the flow features are captured. The drawback of DNS is the computational expense associated with resolving all of the scales of motion. This limits the complexity of the problems that can be tackled. RANS modeling is one alternative where the Navier-Stokes equations are time averaged before a numerical solution is attempted. New unknowns are produced by time averaging that give rise to a closure problem. Closure can be obtained by developing and solving new equations, such as partial differential equations for the conservation of turbulent kinetic energy and dissipation rate (e.g. k-ε model). RANS solutions inherently model all scales, and therefore can only simulate steady flow, or flows that vary in time at a rate much lower that the largest time scales of the turbulent flow. LES is a hybrid method located between DNS and RANS where the large energy containing scales are explicitly solved, while the smaller dissipative scales are modeled. These scales are separated by applying a spatial filter to the Navier-Stokes equations to obtain the filtered Navier-Stokes equations. Similar to RANS new unknowns are produced by the filter and must be solved with new equations. This is accomplished by developing a model similar to a RANS model. However, the model is much simpler than complex RANS modeling such as the k-ε model. It is valid to use a simple model because only the small dissipative

scales that behave in a nearly isotropic manner are modeled. LES has the advantages of capturing the dynamics of the solution similar to DNS, while having a significantly less computational expense.

### 2.4.1. Large Eddy Simulation

The fundamental premise of large eddy simulation (LES) is to explicitly solve the governing equations over large scales (resolved scales) while modeling smaller scales (sub grid scales). By explicitly solving the resolved scales, the full dynamics of the turbulent motion is produced by the large scales is captured. Separation of the resolved and sub grid scales is achieved by applying a spatial filter to the governing equations. In our case, a top hat filter, based on grid size, is applied to the governing equations. By using a filter base on grid size, the resolution of the computation grid sets the filter width. That is, scales of motion larger that the grid size are resolved, and scales smaller than the grid size are modeled. However, in order to fully resolve a specific length scale, one should use several cells smaller that the specific length scales. LES is only valid in flows where the resolved scales dominate the feature that is to be captured. Sub-grid stress (SGS) models are usually simple parameterizations, and are valid for small length scales that are isotropic. In order for an LES computation to be valid, the dominating scales of motion must be resolved by the computational grid. If these scales cannot be resolved, a traditional RANS type turbulence model should be used where the turbulent viscosity is parameterized in a more suitable method over all the scales.

In atmospheric flows, the dominating length scales in the roughness sub-layer are ($L_u = h$) in the stream-wise direction, and ($L_w = h/3$) in the vertical direction (Finnigan

2000). Important coherent structures exist at these rather large scales. Coherent structures are responsible for the majority of the transport into and out of the canopy. The computational grid must be sufficiently refined to capture these scales. Many other practitioners have applied LES to forest canopy flows with a 2 m x 2 m x 2 m cell sized grid, and have shown that this 2m resolution is sufficient to capture coherent structures above a forest canopy (Shaw and Schumann 1992; Leclerc, Shen et al. 1997; Su, Shaw et al. 1998; Patton, Davis et al. 2001). In the case of pheromone dispersion, the scales that drive meander of the pheromone plume are of interest. These scales are smaller than 2m, however the computational expense of LES must also be considered in grid refinement. The goal of the pheromone dispersion simulations is to capture the meander of the whole plume in the resolved scales, while modeling the internal plume dynamics with the sub grid scale model.

LES is computationally expensive, as the resolved scales decrease the size of the computational cells and time step size must also decrease. In theory, if the computational grid is refined to resolve the smallest scales in the flow, LES approaches direct numerical simulation (DNS). However, when the time step size and cell size decrease, the computational expense increases. Thus, the LES practitioner must balance grid refinement and computational expense in order to make the LES approach feasible. In our case, this means restricting the overall computational domain, the cell resolution, and the time step to fit our computational power. One could generate domains with cell resolutions that take weeks to months to solve, however when considering a specific problem many questions arise related to the time step, cell resolution, and computational domain. A two-fold approach was taken to answer these questions and to ensure the

model was providing reasonable solutions. First, a low Reynolds number channel flow simulation was conducted and is presented in Chapter 4. Well known DNS and LES solutions to low Reynolds number channel flows exist and are readily available (Gullbrand and Chow 2002; Kim 2004). Secondly, the lessons learned in the channel flow simulations were extended to a neutral stability forest canopy flow LES computation. Other published LES computations of canopy flows were also followed to extend the channel flow to canopy flow (Shaw and Schumann 1992; Leclerc, Shen et al. 1997; Su, Shaw et al. 1998; Patton, Davis et al. 2001).

# CHAPTER 3: NUMERICAL METHODS

## 3.1. Overview of Numerical Procedure

CFD is comprised of three main parts, grid generation, solving, and post processing. In this chapter the solving portion of CFD is discussed. The first step in using a CFD solver is determining the specific phenomena to be addressed and determining the equations to be solved. Developing a mathematical model for these equations is the next step in CFD. These non-linear partial differential equations are then discretised into a set of algebraic equations over a finite computational grid and solved.

## 3.2. Equations

### 3.2.1. Filtered Governing Equations

The governing equations consist of conservation equations for mass, momentum, energy, and scalars. When applying the incompressible Navier-Stokes equations to the surface layer over short distances the Coriolis forcing term can be neglected. In the surface layer air density variations are neglected in all terms except in the buoyancy term (White 1991). This satisfies the Boussinesq approximation which allows for the decoupling of the energy equation. Buoyancy forces due to temperature effects are only included as a factor in the gravitational acceleration term in the vertical momentum equation. In LES computations the Navier-Stokes equations are spatially filtered. The general filtering method is

$$\bar{\phi}(x) = \int_D \phi(x')G(x,x')dx', \tag{1}$$

where the over bar represents a filtered variable and G is the filtering function. When using the finite volume technique the filter is explicitly set as a top hat filter based on grid size. The filtering operation for a given cell with a volume V is

$$\bar{\phi}(x) = \frac{1}{V}\int_V \phi(x')dx' \qquad x' \in V, \tag{2}$$

where the filtering function is defined as

$$\begin{aligned} G(x,x') &= 1/V, x' \in V \\ G(x,x') &= 0, x' otherwise \end{aligned}, \tag{3}$$

Applying this filtering operation to the governing equations yields filtered conservation equations. The filtered continuity equation is

$$\frac{\partial \rho}{\partial t} + \frac{\partial}{\partial x_i}(\rho \bar{u}_i) = 0, \text{ or } \frac{\partial}{\partial x_i}(\bar{u}_i) = 0, \tag{4}$$

where $\rho$ is the density, $\bar{u}_i$ is the filtered velocity. The filtered conservation of momentum equations are:

$$\frac{\partial}{\partial t}(\bar{u}_i) + \frac{\partial}{\partial x_j}(\bar{u}_i \bar{u}_j) = -\frac{1}{\rho}\frac{\partial \bar{p}}{\partial x_i} + \frac{\partial}{\partial x_j}\left(\nu \frac{\partial \bar{u}_i}{\partial x_j}\right) - \frac{\partial \tau_{ij}}{\partial x_j} + \delta_{i3}(\beta \Delta\theta)\rho g + S_i, \tag{5}$$

where $p$ is the pressure, $\mu$ is the dynamic viscosity, $\delta_{ij}$ is the Kronecker delta, $g$ is the gravity assumed to be in the negative z direction, $S_i$ is a source term, $\theta$ is the potential temperature, $\beta$ is the thermal expansion coefficient, and $\tau_{ij}$ is the SGS stress tensor defined as

$$\tau_{ij} \equiv \rho\overline{u_i u_j} - \rho\bar{u}_i\bar{u}_j . \tag{6}$$

The filtered conservation of momentum equation is unclosed due to the unknown SGS stress tensor $\tau_{ij}$, which arises from spatially filtering the Navier-Stokes equations. This SGS stress tensor is representative of the small scales of motion that are not explicitly resolved. The small scales are nearly isotropic and mostly dissipative; therefore a simple model can be used to achieve closure.

The filtered energy equation for incompressible flow is written in terms of potential temperature, $\theta$, which remains constant during adiabatic expansion or compression (Dawson 1987). The potential temperature profile is constant for neutral conditions, thus solving the energy equation is not necessary. The filtered energy equation is:

$$\frac{\partial}{\partial t}\left(\bar{\theta}\right) + \frac{\partial}{\partial x_i}\left[\bar{u}_i\bar{\theta}\right] = \frac{\partial}{\partial x_j}\left[\alpha\frac{\partial\bar{\theta}}{\partial x_j}\right] - \frac{\partial\tau_{j\theta}}{\partial x_j} + S_h , \tag{7}$$

where $\bar{\theta}$ is the filtered potential temperature, $S_h$ is a source term, $\alpha$ is the thermal diffusivity written as

$$\alpha = k / \rho c_p , \tag{8}$$

where k is the thermal conductivity, and $c_p$ is the specific heat of air. $\tau_{j\theta}$ is the SGS term defined as

$$\tau_{j\theta} \equiv \rho\overline{\theta u_j} - \rho\bar{\theta}\bar{u}_j , \tag{9}$$

and is formed by filtering the energy equation and represents the unresolved scale. This term must be modeled in order to close the set of equations. The convection-diffusion conservation equation for a tracer species $i$, is

$$\frac{\partial}{\partial t}\left(\rho\bar{Y}_i\right)+\frac{\partial}{\partial x_j}\left(\rho\bar{u}_j\,\bar{Y}_i\right)=-\frac{\partial}{\partial x_i}\left(D_i\,\frac{\partial\bar{Y}_i}{\partial x_i}\right)-\frac{\partial\tau_{jY}}{\partial x_i}+S_i\,, \tag{10}$$

where $S_i$ is a source term, $\bar{Y}_i$ is the local filtered mass fraction of species i, $D_i$ is the diffusion coefficient for species i, and $\tau_{jj}$ is the SGS term defined as

$$\tau_{jY}\equiv\rho\overline{Yu}_j-\rho\bar{Y}\bar{u}_j\,, \tag{11}$$

and is formed by the filtering operation on the conservation equation for species $Y_i$. This SGS term produces more new unknowns which must be modeled in order to form a closed set of equations.

3.2.2. Sub-grid Scale Model

The Smagorinsky-Lilly eddy viscosity SGS model was used in the LES computations. This SGS model is a simple mixing length model, however if one resolves much of the large scales in the flow, the smaller scales are nearly isotropic and a simple SGS model should be adequate. SGS stresses have the following relation

$$\tau_{ij}-\frac{1}{3}\tau_{kk}\delta_{ij}=-2\mu_t\bar{S}_{ij}\,, \tag{12}$$

where $\mu_t$ is the SGS turbulent viscosity, and $\bar{S}_{ij}$ is the resolved scale rate of strain tensor defined by

$$\bar{S}_{ij}=\frac{1}{2}\left(\frac{\partial\bar{u}_i}{\partial x_j}+\frac{\partial\bar{u}_j}{\partial x_i}\right), \tag{13}$$

The Smagorinsky SGS model is fundamentally an eddy viscosity mixing length model where the mixing length scale $L_s$ is calculated as

$$L_s = \min\left(\kappa d, C_s V^{1/3}\right). \tag{14}$$

Very near the wall the length scale is calculated as the product of the von Kármán constant $\kappa$ and the distance from the wall $d$, otherwise the length scale is calculated by the product of the Smagorinsky coefficient $C_s$ and the cell volume $V$. The eddy viscosity is modeled as

$$\mu_t = \rho L_s^2 \left|\bar{S}_{ij}\right|, \tag{15}$$

where $\left|\bar{S}_{ij}\right|$ is defined as

$$\left|\bar{S}_{ij}\right| \equiv \sqrt{2\bar{S}_{ij}\bar{S}_{ij}}\ . \tag{16}$$

Closure for the SGS terms $\tau_{\theta j}$, and $\tau_{Yj}$ (which appear in the filtered conservation equations for energy and mass fraction of species i respectively) is achieved by modifying the above model for eddy viscosity, $\mu_t$, with constant turbulent Prandtl or Schmidt numbers. The turbulent Prandtl number, $\mathrm{Pr}_t$, is set at 0.85, and the turbulent Schmidt number, $Sc_t$, is set at 0.7. This type of closure is called constant Prandtl or Schmidt number closure, where $\tau_{j\theta}$ and $\tau_{jY}$ are modeled as:

$$\tau_{j\theta} = \frac{\mu_t}{\mathrm{Pr}_t}, \tag{17}$$

and

$$\tau_{jY} = \frac{\mu_t}{Sc_t} \tag{18}$$

respectively, where $\mu_t$ is the eddy viscosity determined by the Smagorinsky SGS model.

### 3.3. Canopy Parameterization

A generic loblolly pine canopy was modeled as horizontal homogenous porous media. This particular canopy is found in southern plantations where the timber is grown primarily for pulp. Forest canopies are typically spatially inhomogeneous, but this loblolly pine plantation is relatively homogeneous in the horizontal direction since the stand is even aged and the trees were planted in rows. Porous media was used to simulate the canopy and provide a sink for momentum. The physical geometry is not represented in this approach, instead inertial loss terms are calculated to provide the same net effect on the flow. Inertial loss terms, as a function of height, were calculated from a leaf area index LAI, a stem density of 1521 stems/hectare, and formulated using leaf area density (LAD). By definition LAI is one sided leaf area per unit of ground area ($m^2/m^2$), and LAD is surface area of vegetation per volume of atmosphere ($m^2/m^3$).

Momentum sinks based on LAD, $\alpha_z$, have been well documented by Raupach and Thom (1981); Amiro (1990); and Kaimal and Finnigan (1994), and have the following form

$$S_i = \rho \cdot C_d \cdot \alpha_z \cdot \bar{u}_z^2, \tag{19}$$

where $C_d$ is the effective drag coefficient, $\bar{u}$ is the wind speed at height z, and $\alpha_z$ is the LAD as a function of height. Following Amiro (1990) $C_d$ was set to 0.15. The source term in the momentum equation has the following form for a porous media,

$$S_i = -C_2 \cdot \frac{1}{2} \rho \cdot \overline{u}_{mag} \overline{u}_j \,, \tag{20}$$

where $C_2$ is the inertial loss coefficient, given by

$$C_2(z) = 2 \cdot C_d \cdot \alpha_z \,, \tag{21}$$

and shown in Figure 5. Porous media was also used to represent the trunks of the canopy. Assuming the trunk is a cylinder the individual trunk coefficient of drag, $C_{d_T}$, is 0.9 (White 1991). A coefficient of drag, $C_d$, representing the entire fetch was calculated by

$$H \cdot L \cdot W \cdot C_d = \sum_i (A_T C_{d_T})_i \,, \tag{22}$$

where H, L, W are the height, length, and width of the domain respectively, and $A_T$ is the cross-sectional area of a tree. The coefficient of drag, $C_d$, was then equated directly to the inertial loss coefficient, $C_2$,

$$C_d = \sum_i (A_T C_{d_T})_i \Big/ H \cdot L \cdot W \,. \tag{23}$$

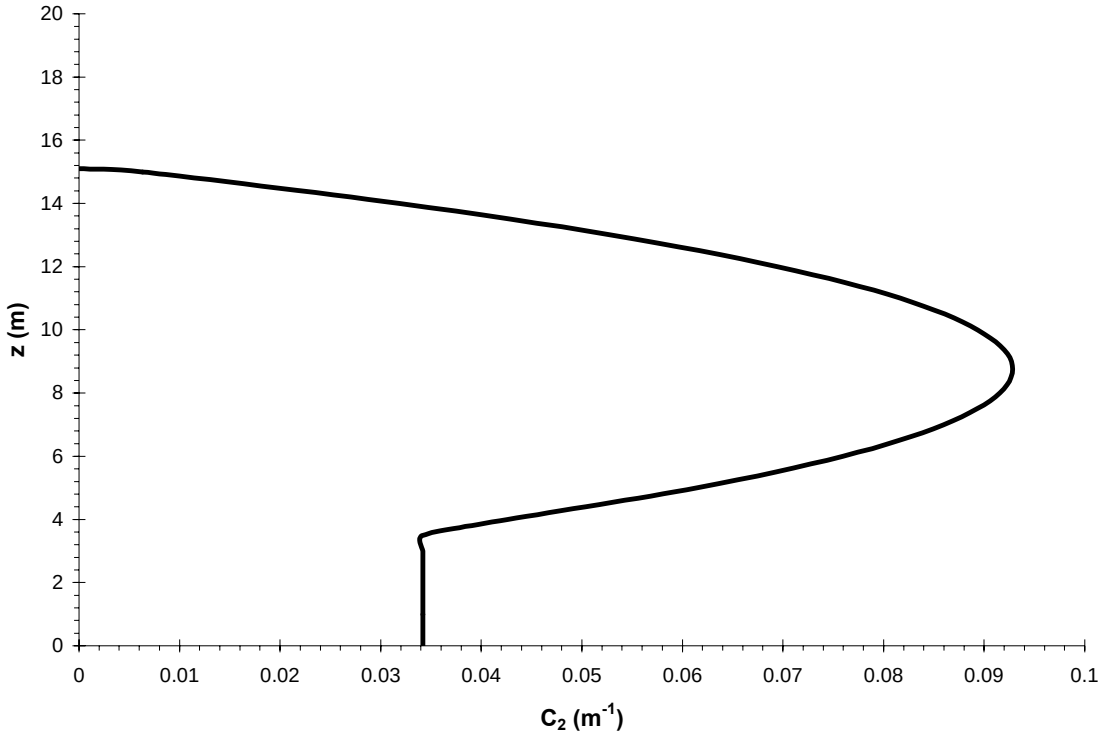


**Figure 5: Profile of the inertial loss coefficient as prescribed for a LAI of 2.1.**

### 3.4. Solar Heating Parameterization

Solar radiation was modeled with a heat source term, $S_h$. The heat source for a cell with a volume $V$ is calculated as

$$S_h(z) = \frac{dQn(z)}{dz} \cdot V \,, \tag{24}$$

with $Qn(z) = Qn(h) \cdot \exp(-aF)$, and the non-dimensional cumulative LAI, $F$, was calculated as $F = \int_z^h \alpha \, dz$. $Qn(h)$ was fixed at 100 W/m$^2$ and $a$, the extinction coefficient, was set to 0.6 following Shen and Leclerc (1997).

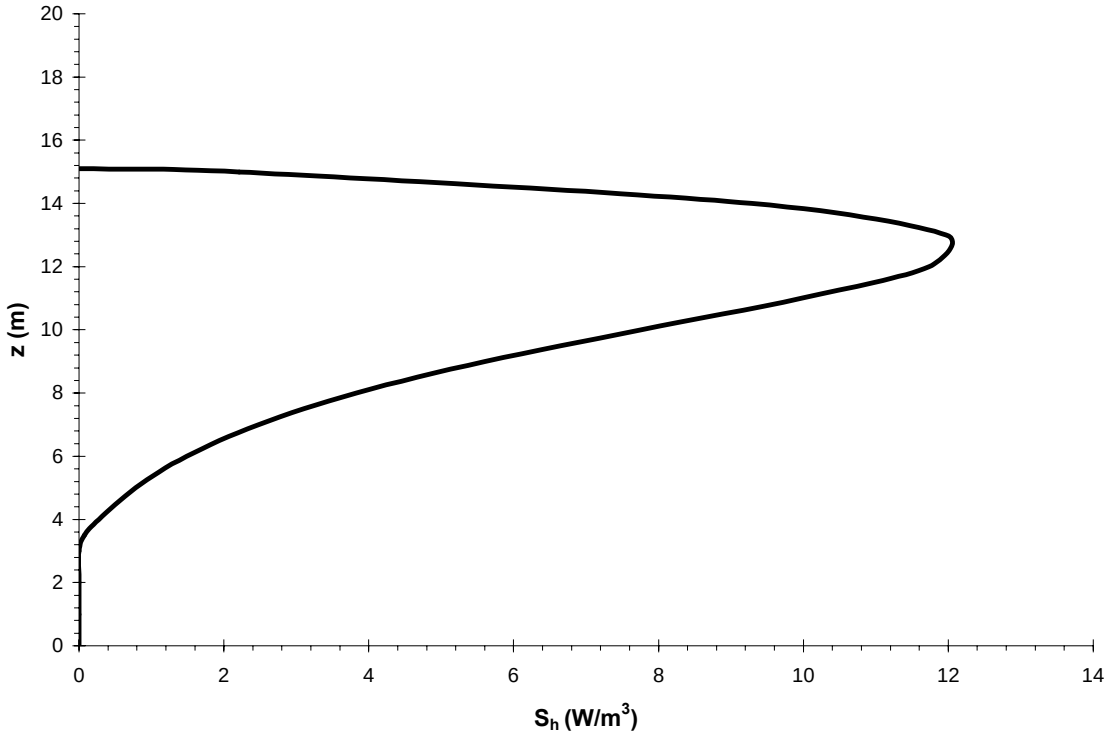


**Figure 6: Profile of the solar heat source as prescribed in the convective condition case.**

## 3.5. The Finite Volume Method

### 3.5.1. Discretisation and Linearization

The governing equations are discretised over a cell centered finite control volume computational grid in order to produce a set of algebraic equations. Numerical diffusion is present in most popular discretisation schemes such as the second order upwind scheme. LES is susceptible to numerical diffusion because it can overwhelm physical diffusion. Therefore, a second order accurate central differencing discretisation scheme was used. It is well known that central differencing schemes are susceptible to unrealistic wiggles in the velocity fields. These wiggles are most prevalent in coarse computational

grids with large time steps. Careful attention was paid to ensure the computations did not produce these unrealistic wiggles.

The finite volume method is based on discretising the integral conservation equations. For example, the diffusion term in integral form is discretised as:

$$\int_V \frac{d}{dx}\left(\Gamma \frac{d\phi}{dx}\right) dV = \left(\Gamma A \frac{d\phi}{dx}\right)_e - \left(\Gamma A \frac{d\phi}{dx}\right)_w \tag{25}$$

where $\Gamma$ is the interface diffusion coefficient, $A$ is the cell face area, $\phi$ is a scalar variable, $V$ is the cell volume, and the subscripts e, and w, represent the cell faces to the right and left, respectively. This requires interpolation of fluxes at the cell faces. On a one dimensional grid, the central differencing discretisation scheme calculates the flux at the face of the cell as:

$$\left(\Gamma A \frac{d\phi}{dx}\right)_e = \Gamma_e A_e \left(\frac{\phi_E - \phi_P}{\Delta x_{PE}}\right) \tag{26}$$

where $\Delta x_{WP}$ represents the distance between neighboring centroids W and P. The flux at face w is written similarly as:

$$\left(\Gamma A \frac{d\phi}{dx}\right)_w = \Gamma_w A_w \left(\frac{\phi_P - \phi_W}{\Delta x_{WP}}\right) \tag{27}$$

The central differencing scheme yields a set of non-linear algebraic equations which are linearized by

$$a_P \phi = \sum_{nb} a_{nb} \phi_{nb} + b\,, \tag{28}$$

where $a_P$ and $a_{nb}$ are linearized coefficients and 'nb' refers to the neighboring cells.

### 3.5.2. Pressure Coupling Algorithm

The Semi Implicit Method for Pressure Linked Equations Consistent (SIMPLEC) algorithm was used to couple pressure and velocity. Coupling between pressure and velocity is achieved by using relationships between velocities and pressure corrections to ensure mass conservation. First initial guesses are used for pressure, velocity, viscosity, and scalars. Next pseudo velocities are calculated, a pressure equation is solved and the pressure is updated. The discretised momentum equations are solved with this new pressure, then a pressure correction equation is solved, and then used to correct the velocities. Finally all other discretised equations are solved and the solution is check for convergence. If the solution does not meet the convergence criteria the calculated pressure, velocity, viscosity, and scalars are updated and the procedure is repeated (Versteeg and Malalasekera 1995). Convergence is determined by checking the residual value against a set minimum, where the residual is defined as an imbalance in the algebraic equations. An example of a residual, for the continuity equation, is the rate of mass creation summed over all cells. This residual should decrease and level off with increasing iterations, thus reaching convergence.

### 3.5.3. Segregated Solver Algorithm

The segregated solver algorithm was used to solve the discretised equations. Figure 7 is a schematic of the time advancement in the segregated solver algorithm. Each outer iteration loop represents one iteration, and each loop after convergence represents one time step. First all properties are updated from the previous iteration or initial conditions. The momentum equations are then solved and the flow field is updated. Next, the pressure algorithm is used to update the pressure and face mass fluxes in order

to satisfy continuity. Finally the energy, species, turbulence, and scalar equations are solved. If the solution is converged the time step is advanced, if not the outer iteration process is repeated until convergence.

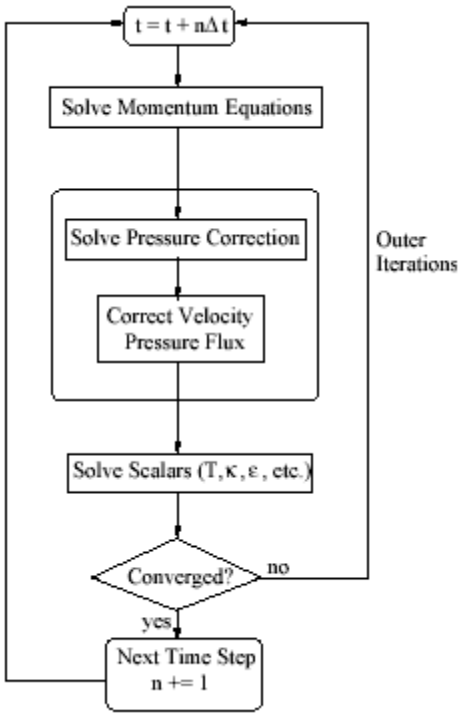


**Figure 7: Schematic of the segregated solver algorithm.**

### 3.5.4. Convergence and Stability

Convergence was ensured by checking normalized residuals at each time step. Residuals can be misleading in many unsteady flows, thus other parameters were monitored to ensure convergence and stability. Shear stress above the canopy, velocities, and temperatures were monitored at each time step. A maximum shear stress above the canopy should exist, mean velocity profiles should exhibit an inflection point above the canopy, instantaneous velocities should be higher above the canopy and lower in the canopy, and mean temperature should decrease with height above the canopy. The

solution should approach a time average steady solution over a finite time due to the boundary conditions imposed. Thus, two independent statistical averages were compared to determine if the solution has reached steady state.

### 3.5.5. Large Eddy Simulation Index of Quality

LES approaches DNS as the computational cell size decreases to the smallest scales of the flow. One test of the quality of an LES solution is quantifying the amount of energy in the SGS. Following Celik (2003), the LES index of quality is defined as:

$$LESIQ = \frac{k^{res}}{k^{tot}} \tag{29}$$

where $k^{res}$ is the resolved kinetic energy, and $k^{tot}$ is the total kinetic energy. In a DNS computation this ratio would be 1. According to Celik (2003) if the LESIQ is above 0.75 the solution is adequate. That is, 75% of the energy is in the resolved scale. This supports the notion that the SGS model can be simple as compared to traditional RANS models because it is only used to model a small portion of the energy. Furthermore, this energy is in the small dissipative energy scales which behave in a nearly isotropic manner.

# CHAPTER 4: CHANNEL FLOW

## 4.1. Fully Developed Turbulent Channel Flow

Before applying a numerical model to a unique engineering problem the scheme should be evaluated against known solutions. CFD involves a large number of options and decisions to be made before a simulation may be run. Questions regarding grid resolution, domain size, initial and boundary conditions, time stepping, statistical sampling, and post-processing can be answered by evaluating a particular simulation with well documented solutions. In our case, a turbulent channel flow simulation was conducted and compared to turbulent wall function laws, LES, and DNS computations

A channel flow simulation with a turbulent Reynolds number of approximately 180 ($Re = u_* H/\nu$) was conducted. A coarse grid with 36 x 36 x 36 (axial x normal x span-wise) cells, and domain size of ($2\pi H$ x $2H$ x $\pi H$) was used for the simulations. The grid size used is rather coarse, with approximately 48,000 cell volumes. However for this preliminary investigation the interest was using a resolution similar to what will be used for canopy flow. A time step of 0.001 s was used, corresponding to $\Delta t^+ = 0.3$ ($\Delta t^+ = \Delta t\ u_*^2 / \nu$). No slip boundaries were used for the normal planes, and the velocity at the first cell off the wall was calculated using a wall function. The first cell off the wall had a wall coordinate value of $y^+ = 1$, in the region of $1 < y^+ < 5$ the well know inner law holds, thus the velocity for the first cell off the wall was calculated using $u^+ = y^+$. Periodic boundary conditions were used in the horizontal directions. A mass flow rate was used to drive the flow, and was determined by integrating the mean velocity profile from a k-ε solution. The mass flow rate was calculated as 0.012 kg/s, an equivalent pressure drop was calculated by using the average wall shear stress across both wall boundaries for a

given time step. A k-ε solution was used as an initial condition for the LES computation. Random fluctuations of 10% of the mean axial velocity were added to each velocity component in the entire computational domain.

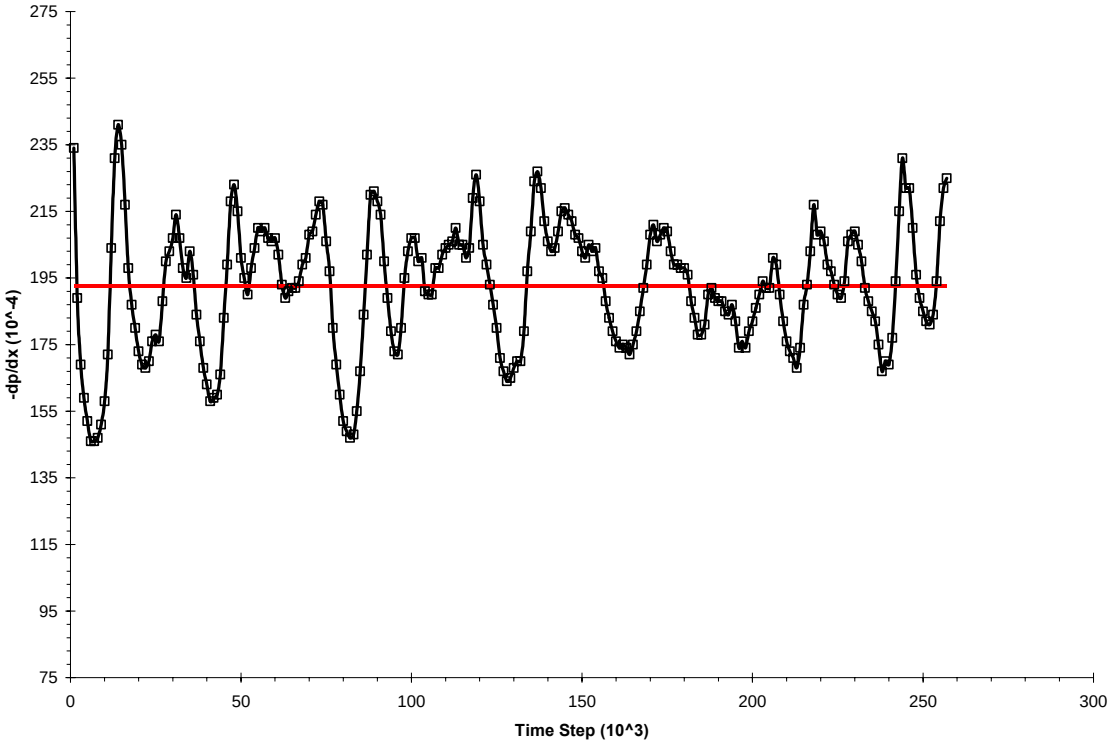


**Figure 8: Time series of pressure drop corresponding to channel flow at a low Reynolds number.**

The calculated pressure drop varied with time in the LES computation. This was expected due to the inherent transient nature of the computation. Figure 8 shows the time series of the pressure gradient. To determine if a steady state solution has been reached in an unsteady computation, one must compare two independent averages. In order to minimize the averaging time, the solution is computed for a significant time period before averaging takes place. In this case, the solution was run for 100,000 time steps before an average was taken. The simulation was sampled and averaged over 50,000 time steps, run for 50,000 time steps, and sampled for another 50,000 time steps. These large

sampling periods were required due to the slow periodic nature of the pressure gradient term Figure 8. This periodicity corresponds directly to the variation of the wall shear stress, which is the primary parameter in a channel flow simulation.

Mean velocity and root mean squared (RMS) profiles for fully developed turbulent channel flow at low Reynolds numbers are well known from both measurements (Wallace, H. Eckelmann et al. 1972), DNS (Kim, Moin et al. 1987), and LES (Kim 2004). Our LES mean and RMS velocity profiles are compared with DNS solutions in Figure 9 and Figure 10. Discrepancies between DNS v' and w' values are due to the Smagorinsky SGS model. The Smagorinsky SGS model is known to be overly dissipative for wall bounded flows.

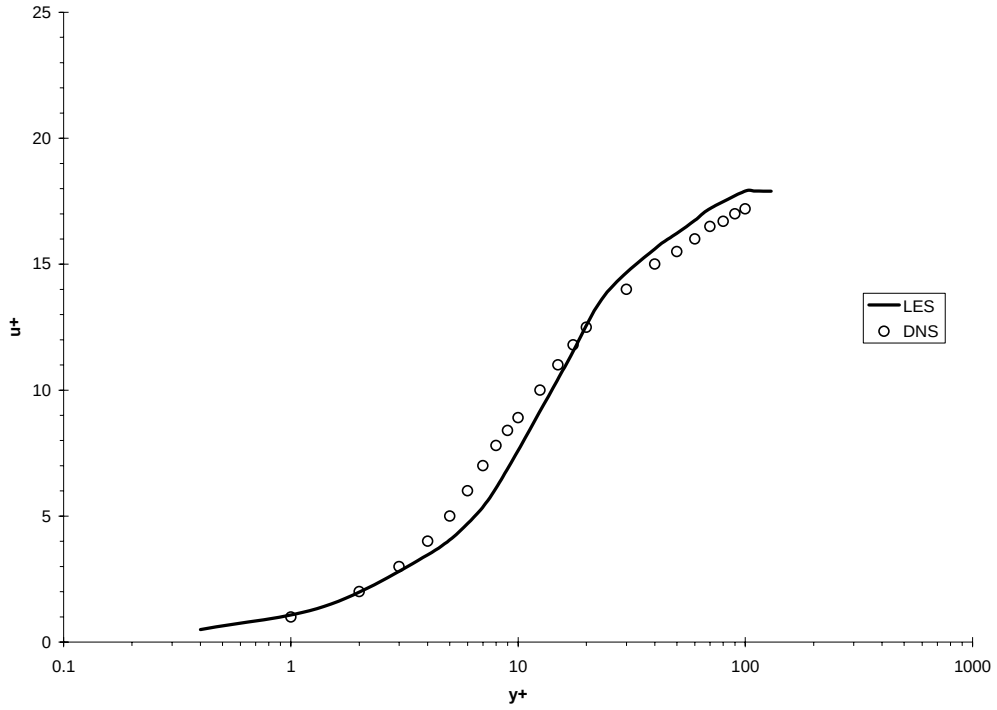


**Figure 9: Mean velocity profile for channel flow at low Reynolds number. u* = 0.030 m/s.**

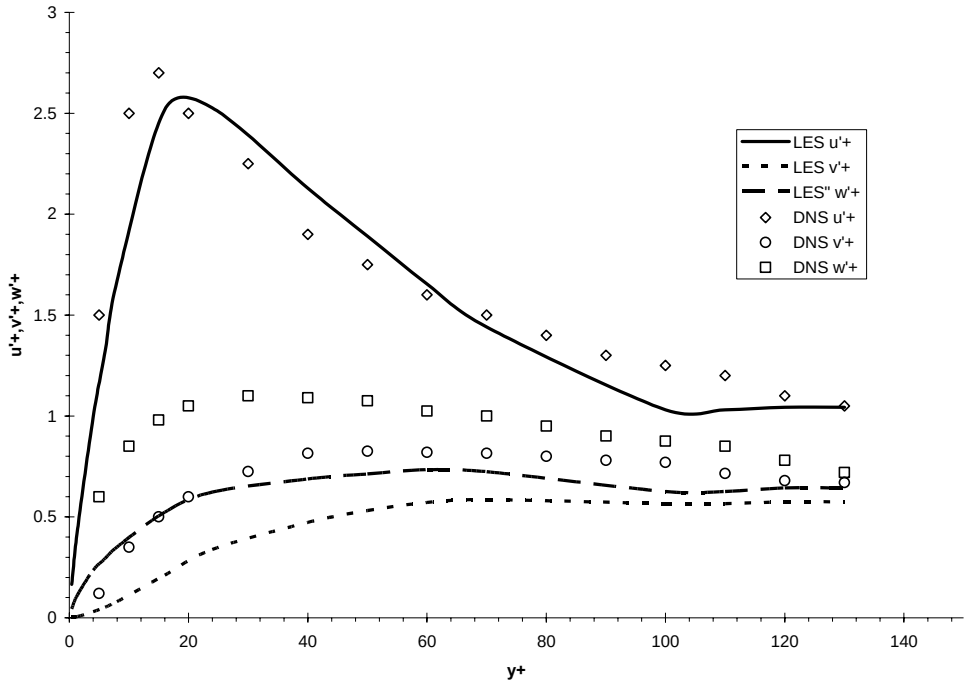


**Figure 10: RMS velocity profiles for channel flow at low Reynolds number. u* = 0.030 m/s.**

It is necessary to ensure the large scale dynamics are captured in this channel flow simulation. Fluctuating stream-wise ($u'$) and vertical ($v'$) velocities are shown in Figure 11 and Figure 12, respectively. It is clear from these figures that the turbulent fluctuations are captured in the flow field. Next, the bursting and sweeping that occurs close to the wall in turbulent channel flow were examined, a quadrant analysis of $u'$ and $v'$ velocities for a cell located far away from the wall ($y^+ \sim 50$) was conducted (Figure 13). Bursting and sweeping do not dominate the flow at this location. Quadrant analysis is shown in Figure 14 for a cell located close to the wall ($y^+ \sim 8$). Here it is clear that the bursting ($u' < 0,\ v' > 0$) and sweeping ($u' > 0,\ v' < 0$) quadrants dominate the velocity signal.

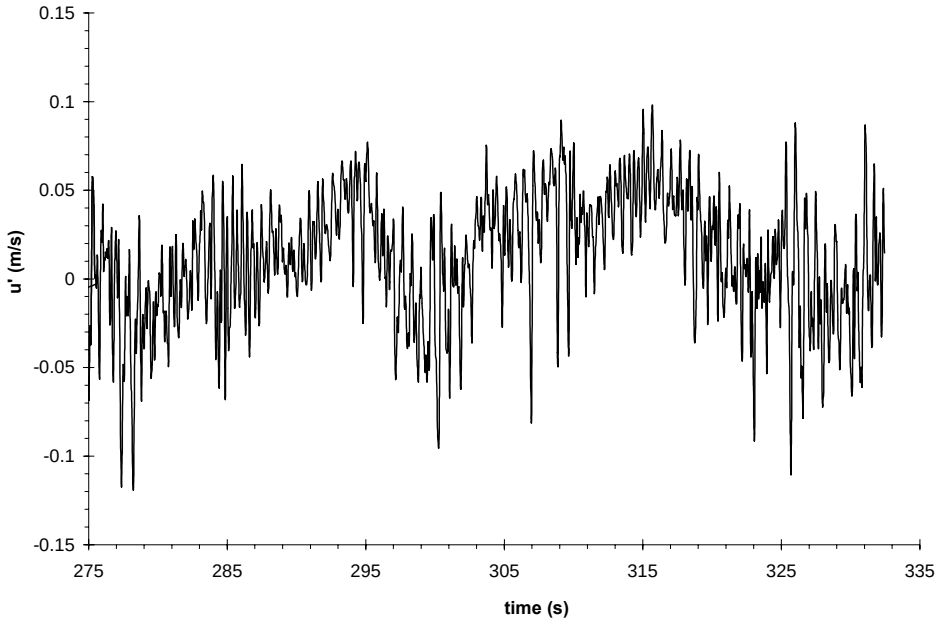


**Figure 11: Stream wise fluctuating velocity signal at $y^+ = 50$ from a turbulent channel flow simulation.**

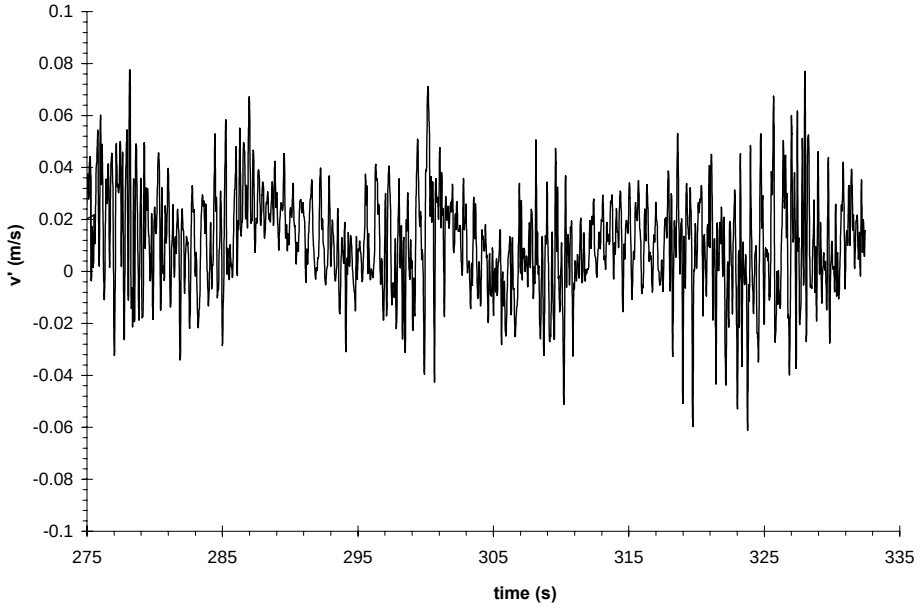


**Figure 12: Vertical fluctuating velocity signal at $y^+ = 50$ from a turbulent channel flow simulation.**

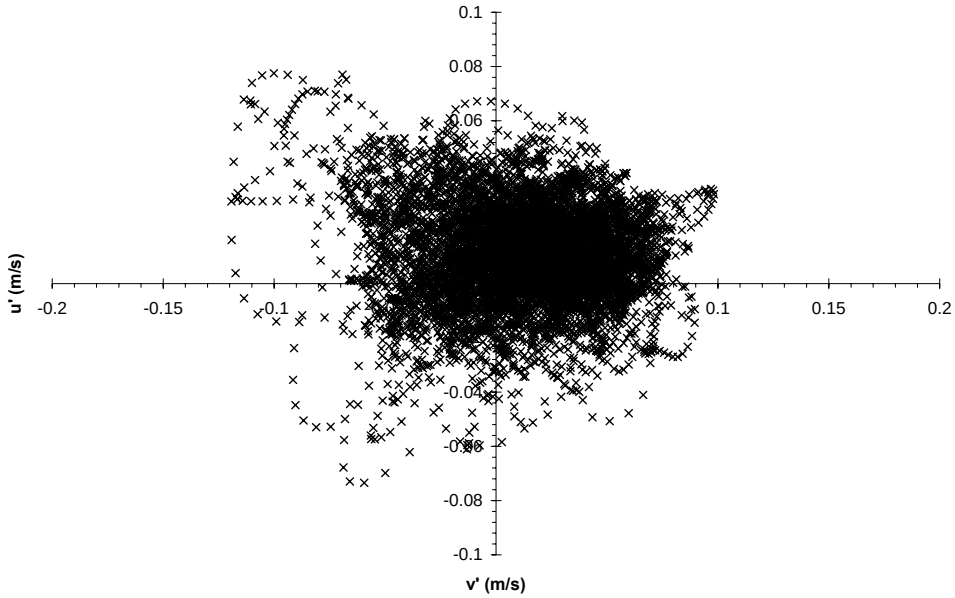


**Figure 13: Quadrant analysis from velocity signal located at $y^+ = 50$ in a turbulent channel flow simulation.**

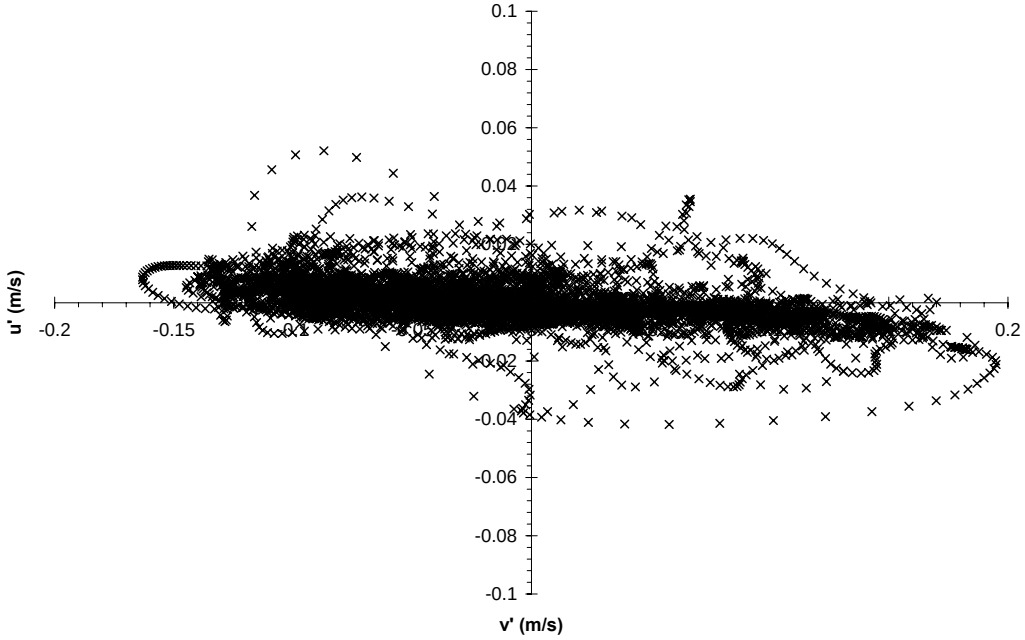


**Figure 14: Quadrant analysis from velocity signal located at $y^+ = 8$ in a turbulent channel flow simulation.**

It was unclear at the beginning of this case study how long the simulation would take to run. Initially it was thought steady state would be reached in a few thousand time steps. However, after plotting the time series of the pressure gradient, it was clear that low frequency variations in the wall shear stress were inherent in the simulation. This required long averaging times, and hence long simulation run times. The channel flow simulation took approximately 15 days of continuous run on a 3 GHz single processor.

This simulation gave insight into LES, initial and boundary conditions, time stepping and post processing. It allowed the testing of different methods to start the LES computations. Different methods for adding random perturbations or fluctuations to the simulation were tested. Correlated random perturbations are preferred, however random fluctuations proved to be sufficient in this case. This may have an effect on the time required to reach a steady simulation. Periodic boundary conditions require the specification of either a mass flow rate or a pressure gradient. Specifying either parameter ultimately produces the same outcome. Furthermore, specifying a mass flow rate requires the monitoring of the pressure gradient fluctuations while specifying a pressure gradient requires the monitoring of the average wall shear stress fluctuations. Monitoring these parameters is necessary to determine low frequency oscillations and ultimately averaging time required to reach a steady state solution.

Moving from a channel flow solution to a forest canopy simulation is not straight forward, however many of the lessons learned in the channel flow case can be directly applied to the forest canopy simulations. These include starting a simulation from a k-ε converged solution with random perturbations added, monitoring wall shear stress and/or

pressure gradient fluctuations with time, allowing the simulation to run far longer than initially assumed, and post processing with similar methods.

# CHAPTER 5: CASE STUDIES

## 5.1. Loblolly Pine Canopy

Two case studies were evaluated corresponding to a Loblolly pine canopy. The first case is a LES of canopy flow during neutral atmospheric conditions and the second case is a LES of canopy flow during convective atmospheric conditions. Each case had similar domain size and grid resolution, as well as initial and boundary conditions. The one difference was that a heat source term within the canopy, and a heat flux upper boundary condition of -5 $W/m^2$ was prescribed for the convective atmospheric case.

### 5.1.1. Domain Size and Grid Resolution

A computational domain of 3h x 2h x 3h (height, width, length) (canopy height, h = 15 m) was used for the LES computations. This domain size was chosen to resolve the scales of the roughness sub-layer and to cover at least 30 m down stream plume dispersion distance, and 30m crosswind horizontal plume motion. The grid resolution in the canopy was approximately 0.8 m, with the cell growth varying from 0.5 m to 1.2 m above the canopy. The sub-grid filter length is shown in Figure 15. Length scales in the canopy and roughness sublayer are h and h/3, therefore the resolution in the canopy and roughness sub-layer is sufficient. Furthermore, previous LES solutions of canopy flow were performed on computational grids having 2 m resolution (Shaw and Schumann 1992; Shaw and Patton 2003).

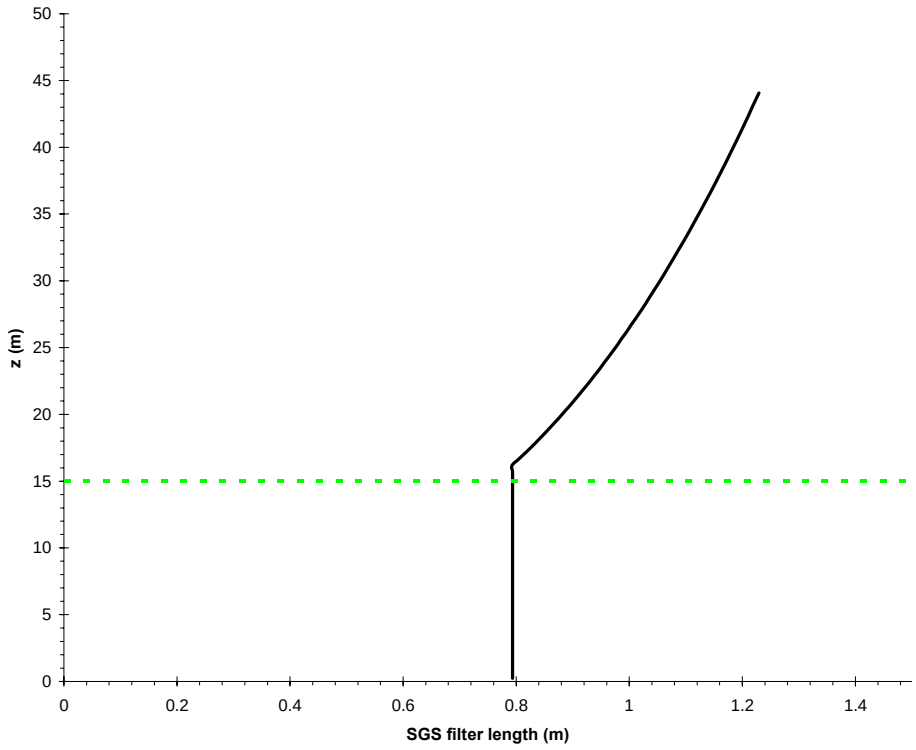


**Figure 15: SGS filter length representing cell resolution as a function of height.**

### 5.1.2. Initial and Boundary Conditions

Random perturbations of 10% of the mean stream-wise velocity were added to each component of velocity from a k-ε solution and used as initial conditions for the LES computation. The lower boundary condition was set as a no-slip wall with a roughness height of 1 m. The law of the wall was used to set the velocity at the first node. Periodic boundaries were used in the horizontal directions with a mass flow rate specified, from which a pressure drop was calculated based on the average wall shear stress. A symmetry plane was used for the top boundary condition in the neutral stability case. A heat flux of -5 $W/m^2$ was prescribed to the upper boundary condition for the convective

stability case. This boundary condition is required to ensure physical potential temperatures..

5.1.3. Source Term: Field and LES

The source term prescribed in the LES cases was 0.1 g/s. This is higher than the experimental release rate of 0.0016 g/s on May 25th 2005 in Winnfield LA. A factor of 62.5 was used to normalize the predicted concentrations in order to make valid comparison with observations. Sonic data for May 25th 2005 is shown in Table 1 to give insight into the variation of wind speed (WS), wind direction (WD), and temperature (Temp) throughout the 4.5 hour sampling period.

**Table 1: Sonic data for May 25th 2005.**

| z = 1.5m (sonic at release) | | | | z = 2.5m (lower sonic on tower) | | | |
|---|---|---|---|---|---|---|---|
| time (CDT) | WS (m/s) | WD (°) | Temp (°C) | time (CDT) | WS (m/s) | WD (°) | Temp (°C) |
| 630 | 0.027 | 66.47 | 24.15 | 630 | 0.123 | 142.35 | 23.74 |
| 700 | 0.085 | 272 | 24.33 | 700 | 0.053 | 347.22 | 23.94 |
| 730 | 0.247 | 278.9 | 24.74 | 730 | 0.219 | 330.14 | 24.33 |
| 800 | 0.144 | 84.07 | 25.2 | 800 | 0.182 | 142.52 | 24.77 |
| 830 | 0.044 | 32.59 | 26.35 | 830 | 0.08 | 174.45 | 25.88 |
| 900 | 0.134 | 60.92 | 27.03 | 900 | 0.118 | 139.13 | 26.61 |
| 930 | 0.069 | 36.2 | 27.67 | 930 | 0.138 | 187.26 | 27.06 |
| 1000 | 0.087 | 154.7 | 28.14 | 1000 | 0.18 | 214.4 | 27.5 |
| 1030 | 0.05 | 198.8 | 29.12 | 1030 | 0.1 | 229.54 | 28.55 |
| 1100 | 0.161 | 235.5 | 29.5 | 1100 | 0.21 | 223.55 | 28.8 |
| z = 1.5m (middle sonic on tower) | | | | z = 25.2m (upper sonic on tower) | | | |
| time (CDT) | WS (m/s) | WD (°) | Temp (°C) | time (CDT) | WS (m/s) | WD (°) | Temp (°C) |
| 630 | 0.499 | 207.86 | 22.74 | 630 | 1.198 | 213.68 | 23.61 |
| 700 | 0.631 | 221.15 | 22.91 | 700 | 1.47 | 226.32 | 23.77 |
| 730 | 0.562 | 235.09 | 23.31 | 730 | 1.294 | 234.13 | 24.12 |
| 800 | N/A | N/A | N/A | 800 | 1.685 | 216.4 | 24.56 |
| 830 | 0.859 | 208.53 | 24.75 | 830 | 1.75 | 213.23 | 25.48 |
| 900 | 0.876 | 198.45 | 25.39 | 900 | 2.033 | 199.69 | 26.07 |
| 930 | 1.26 | 186.73 | 25.81 | 930 | 2.62 | 192.41 | 26.51 |
| 1000 | 1.2 | 194.57 | 26.23 | 1000 | 2.66 | 196.85 | 26.94 |
| 1030 | 1.09 | 201.06 | 27.15 | 1030 | 2.39 | 199 | 27.77 |
| 1100 | 1.14 | 200 | 27.39 | 1100 | 2.44 | 205.87 | 28.04 |

# CHAPTER 6: RESULTS AND DISCUSSION

## 6.1. Loblolly Pine Canopy during Neutral Stability Conditions

Figure 16 shows a mean stream-wise velocity profile from the neutral atmospheric stability case. The data points in Figure 16 correspond to 30 minute averaged observations from sonic anemometer data, and 15 minute averaged observations from SODAR data occurring on May 25$^{th}$ 2005 from 1000 to 1100. The LES solution gives higher velocities inside the canopy and lower velocities above the canopy when compared with observations. However, the general characteristics of canopy flow are reproduced in both the mean velocity (Figure 16) and RMS vertical velocity (Figure 17). These characteristics include an inflection point in mean velocity at the canopy height (h = 15 m), a secondary flow in the under-story of the canopy, and a maximum vertical RMS velocity at the canopy height (h = 15 m).

One to one agreement between observations and modeled profiles are not expected due to the sparseness and spatial variation of the observational data. The first level of data points in Figure 16 (z = 1.5 m) correspond to a sonic located at the release, the next three levels of data points (z = 2.5, 15, 25 m) correspond to sonics located on the tower on the 30 m arc and the final level of data points (z = 40 m) correspond to the SODAR measurements located several miles from the site. Furthermore, better agreement between the simulation and observations can be obtained by modifying the drag coefficient in the porosity formulation.

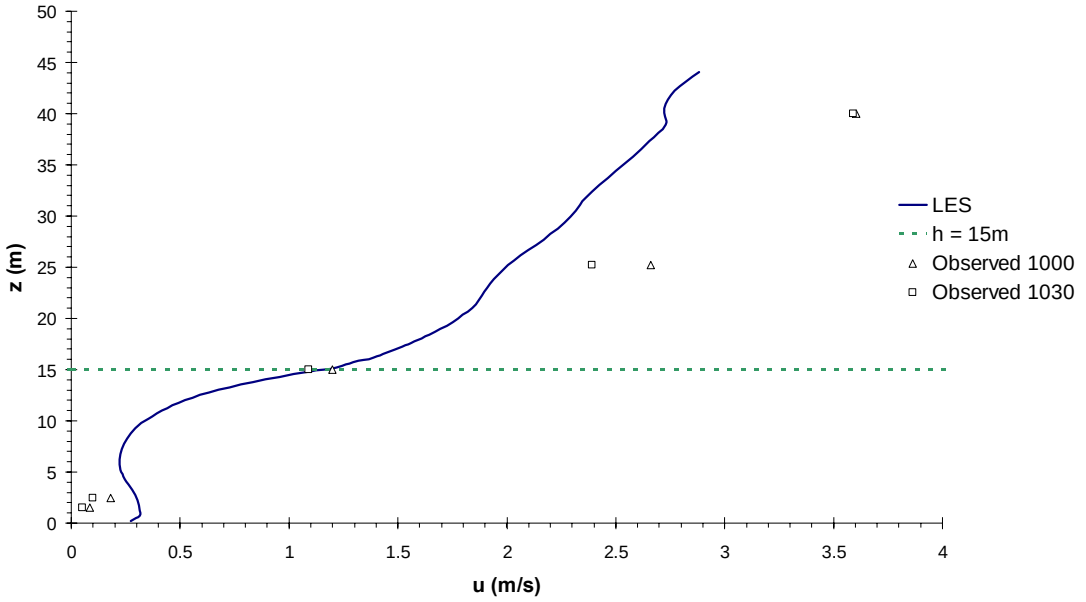


**Figure 16: Mean stream-wise velocity profile evaluated with sonic and SODAR averaged observed velocities from a neutral condition LES.**

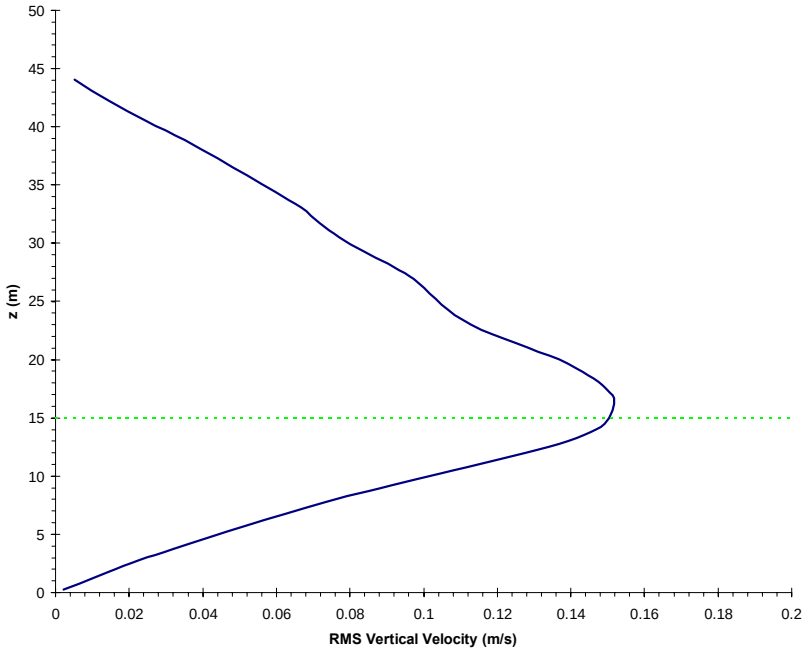


**Figure 17: Root mean squared vertical velocity profile from a neutral condition LES.**

Figure 18: shows snap shots of contours of $SF_6$ mass fraction overlaid on velocity vectors located on a vertical plane at y = 15 m. A coherent structure, with a length scale of approximately h/3, can be seen traveling through the domain. Snap shots of vectors and concentrations of $SF_6$ are also shown on horizontal planes (Figure 21, Figure 20, and Figure 19). Coherent structures with length scales of approximately h/3 exist and influence the tracer gas transport. There is minimal vertical and horizontal transport of the plume.

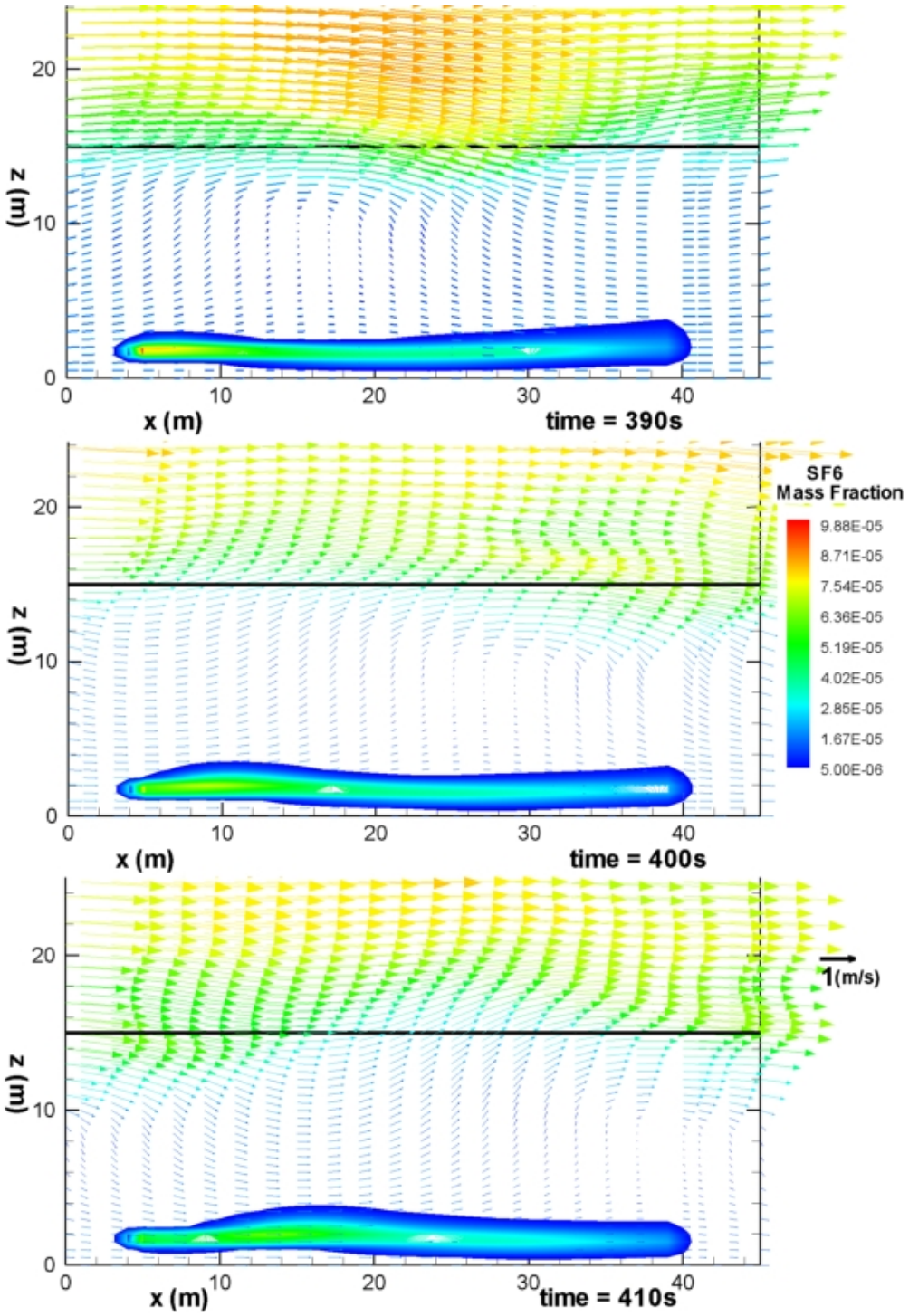


**Figure 18: Contours of $SF_6$ mass fraction overlaid on velocity vectors on a vertical plane located at y = 15 m from a neutral condition LES.**

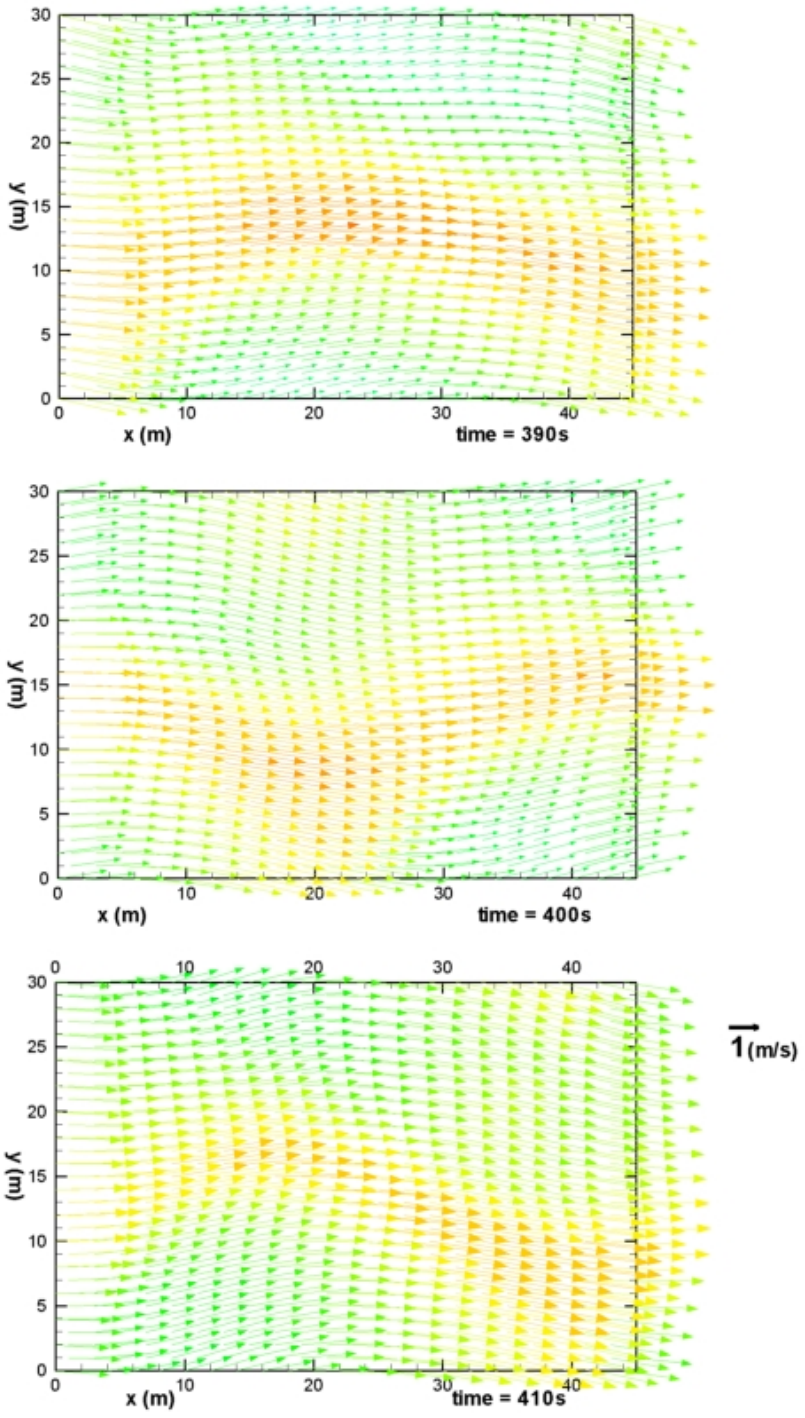


**Figure 19: Velocity vectors on a horizontal plane located at z = 25 m from a neutral condition LES.**

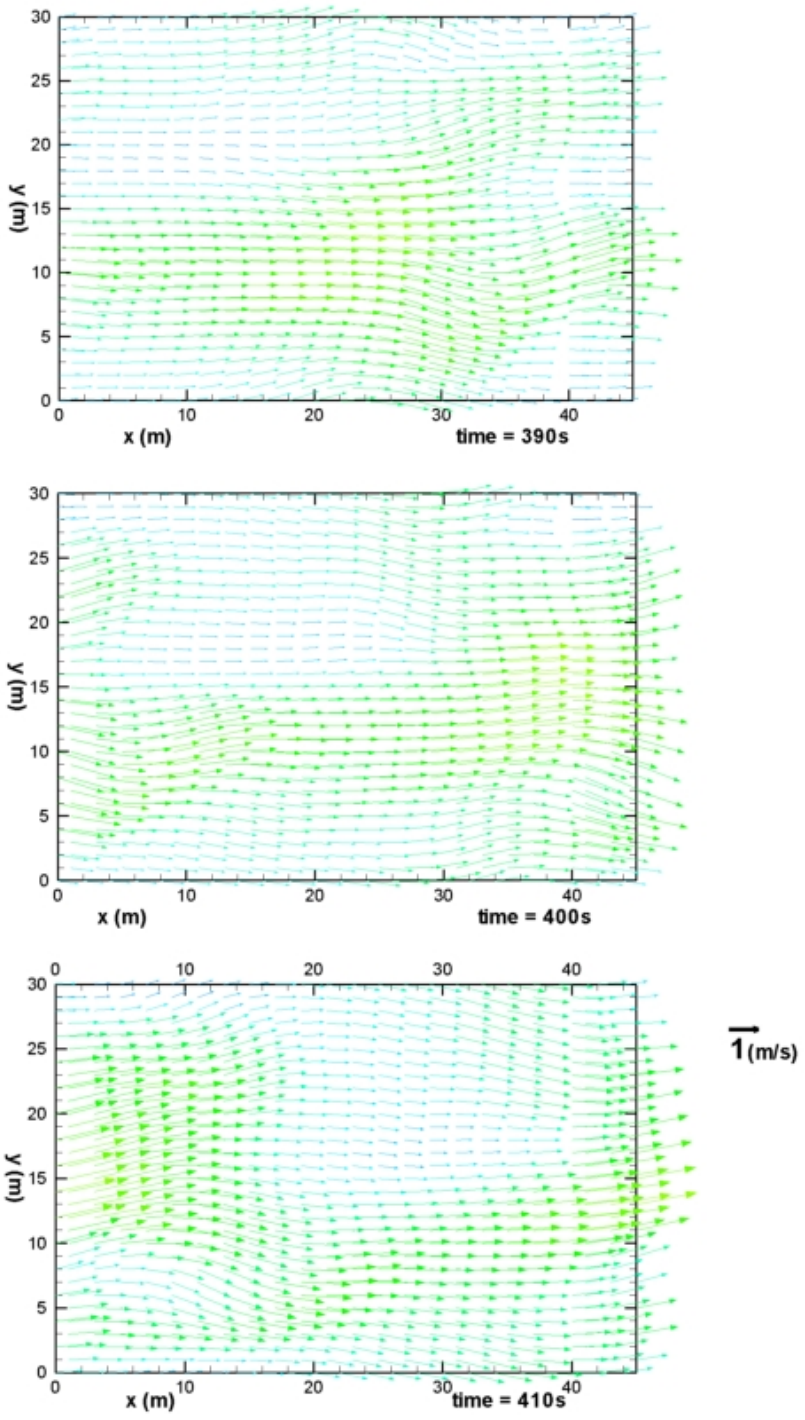


**Figure 20: Velocity vectors on a horizontal plane located at z = 15 m, from a neutral condition LES.**

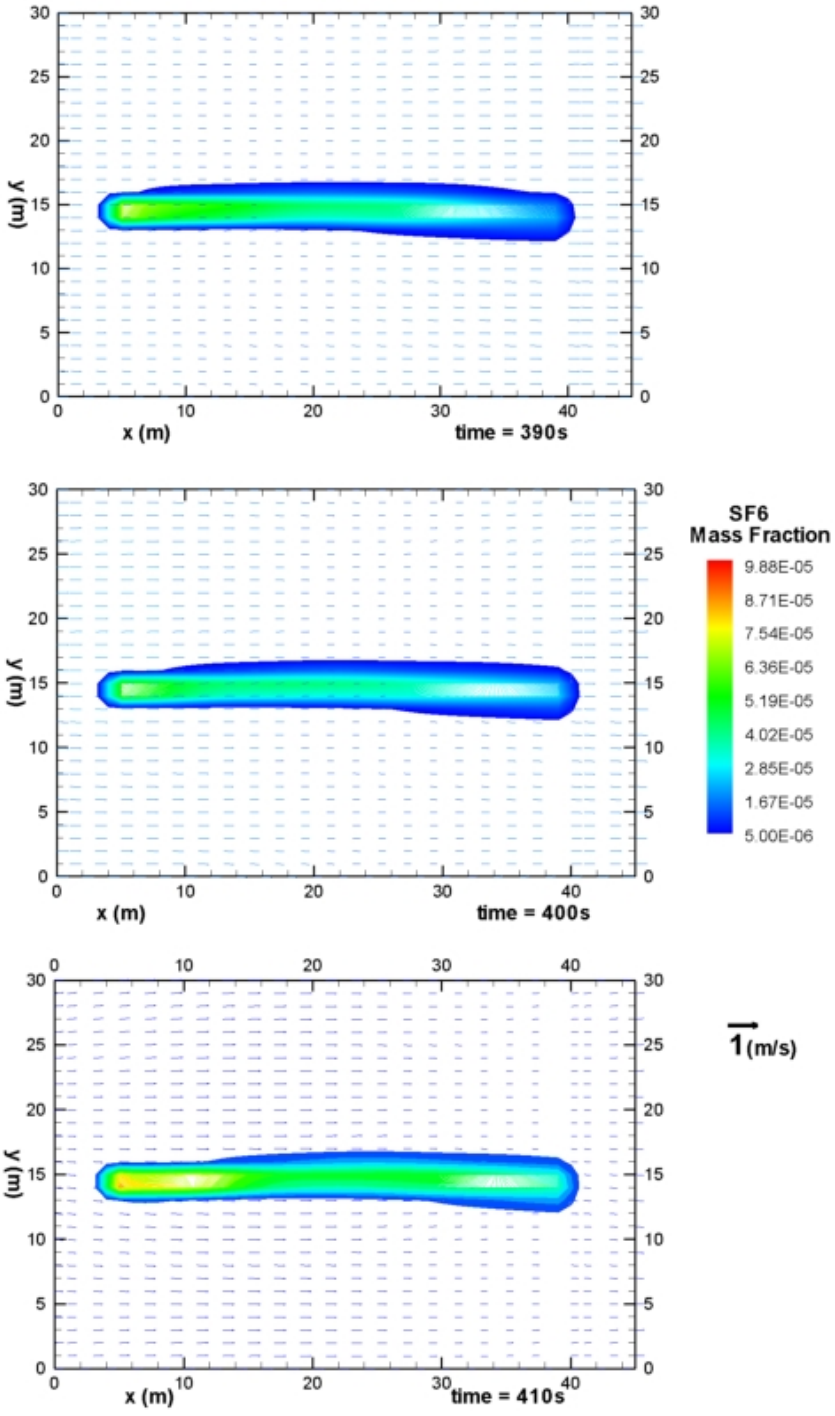


**Figure 21: Contours of $SF_6$ mass fraction overlaid on velocity vectors located on a horizontal plane at z = 1.5 m, from a neutral condition LES.**

Stream-wise and vertical fluctuating velocity signals from single computational grid cells are shown in Figure 22 and Figure 23, respectively. These signals are

compared with sonic anemometer data at the canopy top (z = h= 15 m). LES inherently averages the instantaneous velocity signal over the finite size of the cell. The averaging time is determined by calculating the time it takes for an air parcel to move through a computational cell. In the canopy, the cell size is 0.8 m and the mean vertical velocity is approximately 0.3 m/s, thus the averaging time is approximately 3 seconds. The sonic signal must be averaged in a similar fashion since the sonic receivers have a smaller measuring volume (typically 15 cm) compared to the computational cell size. Both the raw sonic signal, and a 10 s averaged signal are shown in the evaluation of the LES single cell signal (Figure 22 and Figure 23). The dynamics in LES exhibit behavior similar to that measured. In both Figure 22 and Figure 23 the LES signal is lower in amplitude than that of the averaged sonic signal. Observations corresponding to a neutral case were not found in the Louisiana field study data set. This is due to the sparseness of temperature data. Two levels of reliable temperature measurements were collect from two meteorological stations. This did not provide a clear picture of the atmospheric stability.

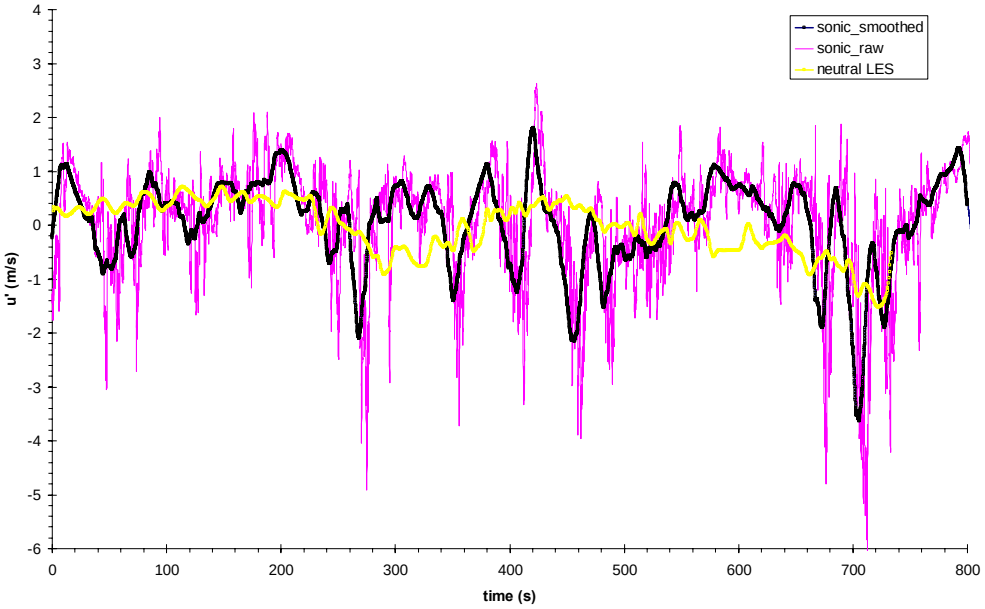


**Figure 22: Fluctuating stream wise velocities from a sonic anemometer, an averaged sonic signal, and neutral condition LES located at the canopy height = 15 m. (** $\overline{u'^2}_{raw} = 0.92$ **m/s,** $\overline{u'^2}_{smoothed} = 0.52$ **m/s,** $\overline{u'^2}_{LES} = 0.23$ **m/s)**

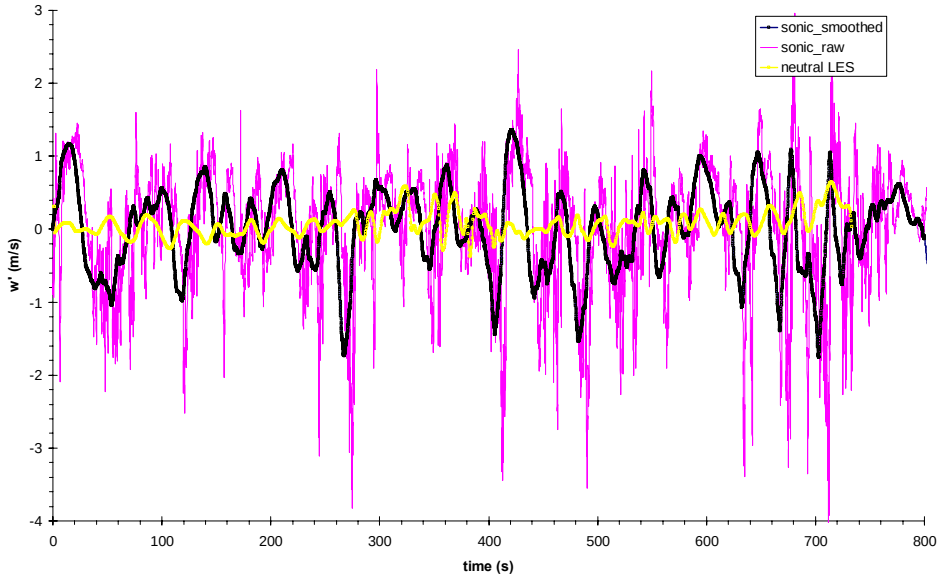


**Figure 23: Fluctuating vertical velocities from a sonic anemometer, an averaged sonic signal, and neutral condition LES located at the canopy height = 15 m. (** $\overline{w'^2}_{raw} = 0.69$ **m/s,** $\overline{w'^2}_{smoothed} = 0.30$ **m/s,** $\overline{w'^2}_{LES} = 0.03$ **m/s)**

Quadrant analysis was performed on a two single cell velocity signals, one located above the canopy at 25 m, Figure 24, and the other located at the canopy height (z = h = 15 m) Figure 25. Bursting and sweeping is explicitly shown to exist at the canopy height (Figure 25).

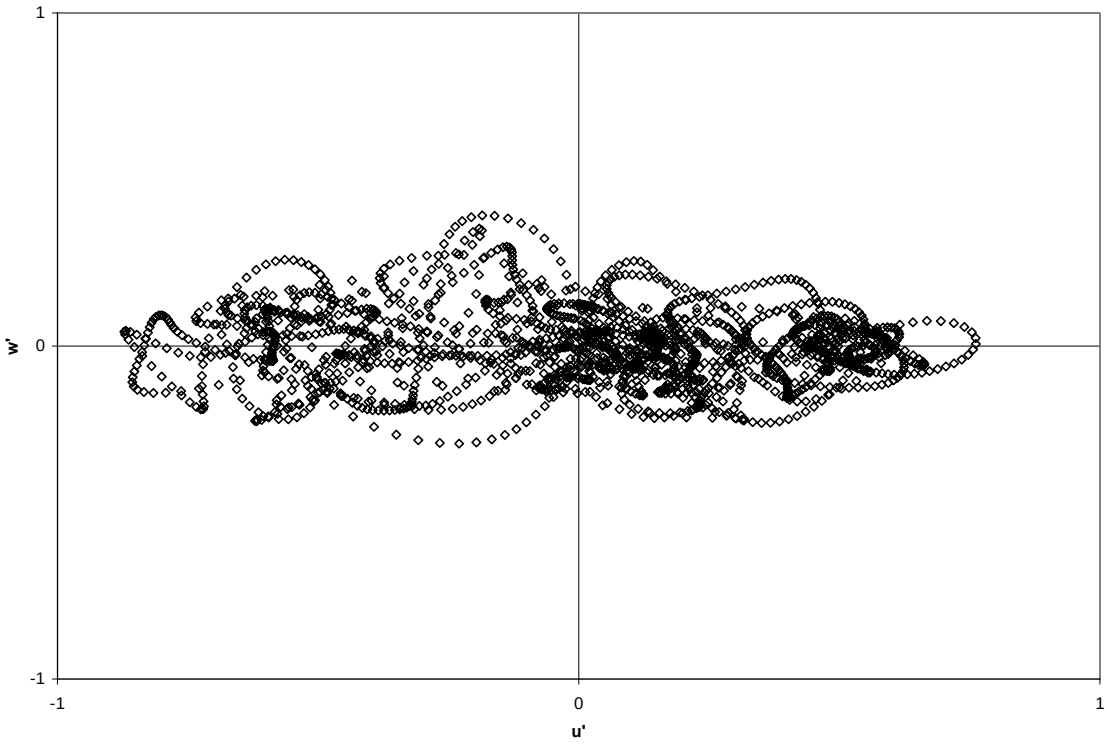


**Figure 24: Quadrant analysis of LES velocity signal located at z = 1.6h (z = 25 m) from a neutral condition LES.**

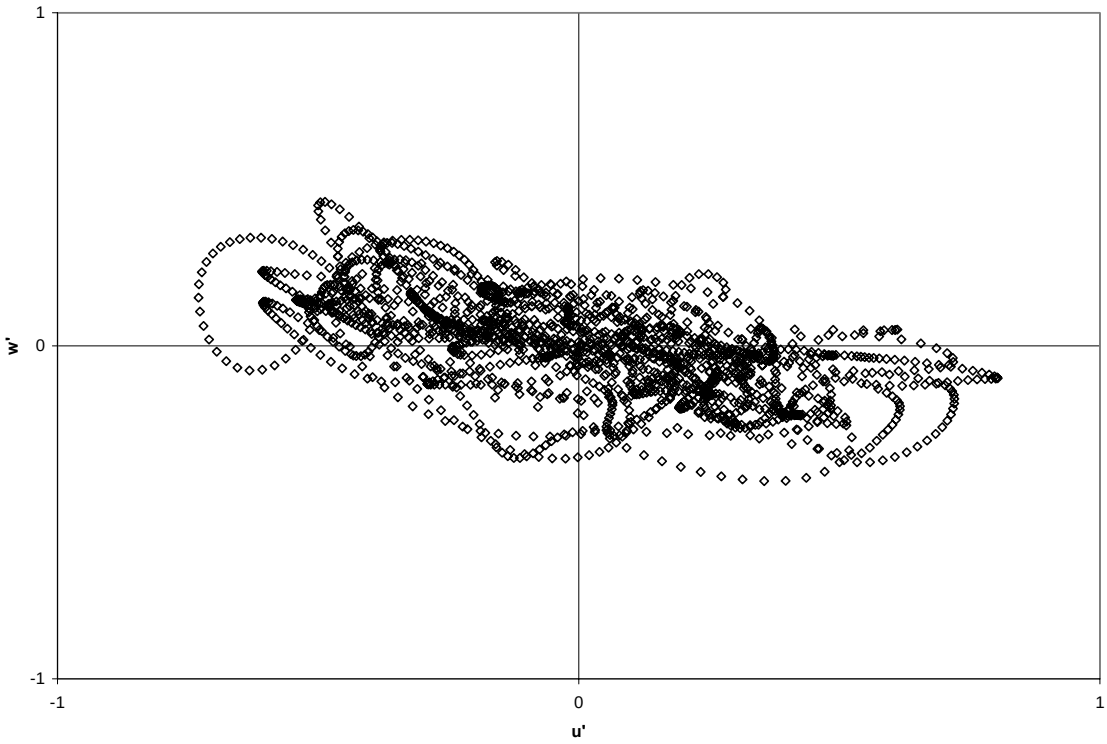


**Figure 25: Quadrant analysis of LES velocity signal located at z = h = 15 m from a neutral condition LES.**

## 6.2. Loblolly Pine Canopy during Convective Conditions

A heat source term was added to the energy equation based on solar absorption within the canopy to simulate convective conditions in a Loblolly pine canopy. Mean velocities are shown in Figure 26. A shear region exists directly above the canopy, and a secondary flow is present in the under story of the canopy. Vertical RMS velocity is shown in Figure 27. A maximum RMS vertical velocity exists at the top of the canopy and decreases with height. Figure 28 shows normalized mean potential temperature as a function of height. The potential temperature increases from the ground to the canopy height, and decreases with height above the canopy height (h = 15 m).

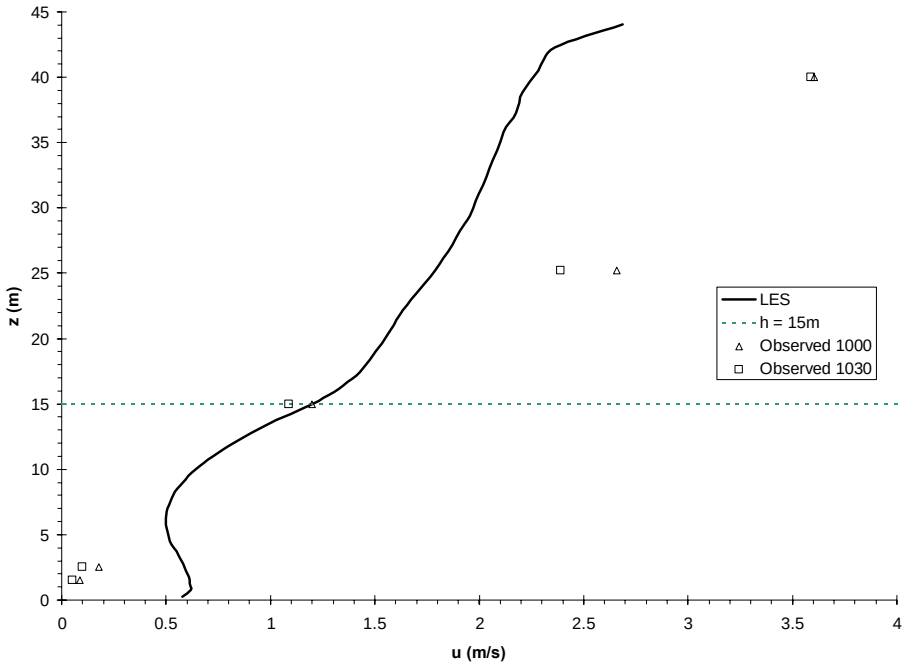


**Figure 26: Mean stream-wise velocity profile evaluated with sonic and SODAR averaged observed velocities from a convective condition LES.**

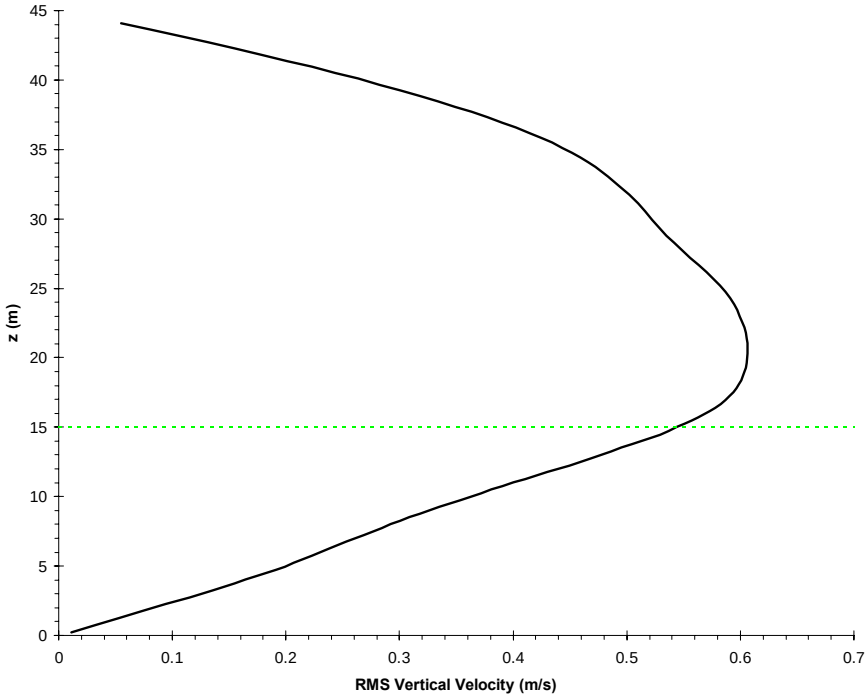


**Figure 27: Root mean squared vertical velocity profile from a convective condition LES.**

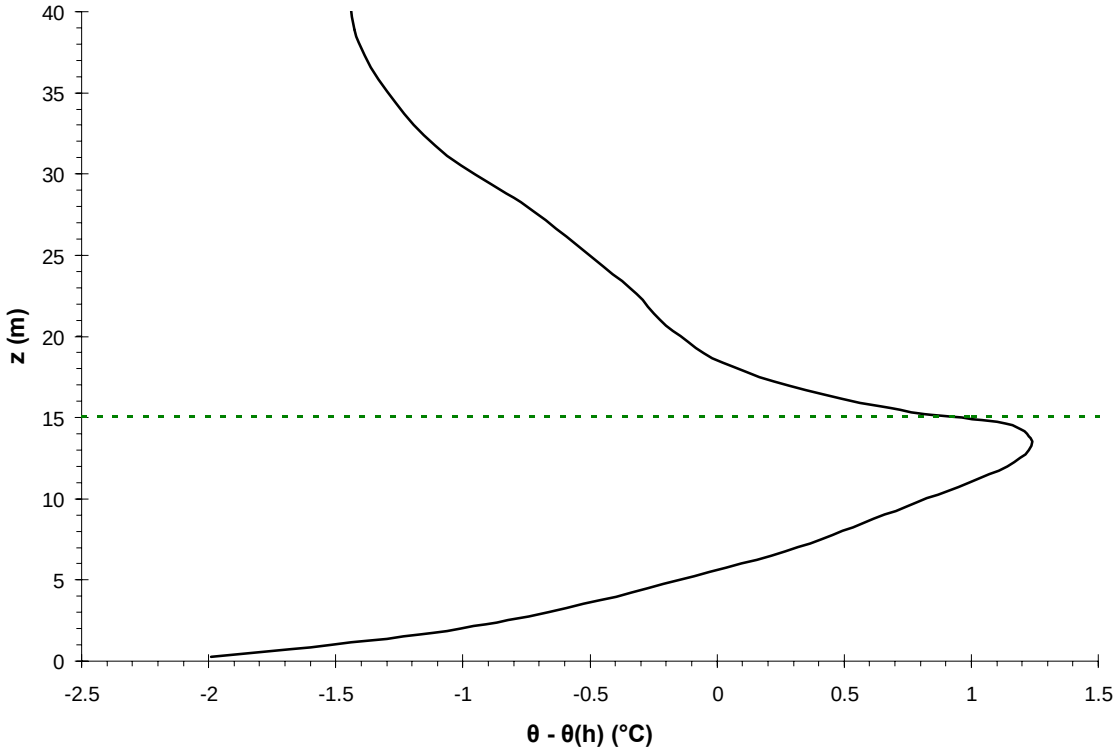


**Figure 28: Mean potential temperature difference profile from a convective LES. Potential temperature difference is calculated by subtracting the potential temperature at the top of the canopy θ(h) = 28 °C ( h = 15 m).**

To demonstrate the influence of convective conditions on the velocity and concentration fields, snap shots of $SF_6$ contours overlaid on velocity vectors located on a vertical plane at y =15 m are shown in Figure 29. During the first snap shot at a time of 1240 seconds the plume is being carried downward by a sweep just after the release point. After 15 seconds, time = 1255 s, the plume is lifted by a burst, and after 30 seconds, time = 1270 s, the plume encounters another downward sweep. Figure 32 shows contours of $SF_6$ overlaid with velocity vectors located on a horizontal plane at z = 1.5 m. The plume is shown to have horizontal motion occurring over the 45 seconds shown; however, most of the plume transport is vertical. Velocity vectors shown on horizontal planes located at

z = 15 m and z = 25 m are shown in Figure 31 and Figure 30 respectively. The velocity vectors have more horizontal motion at these heights as compared to Figure 32.

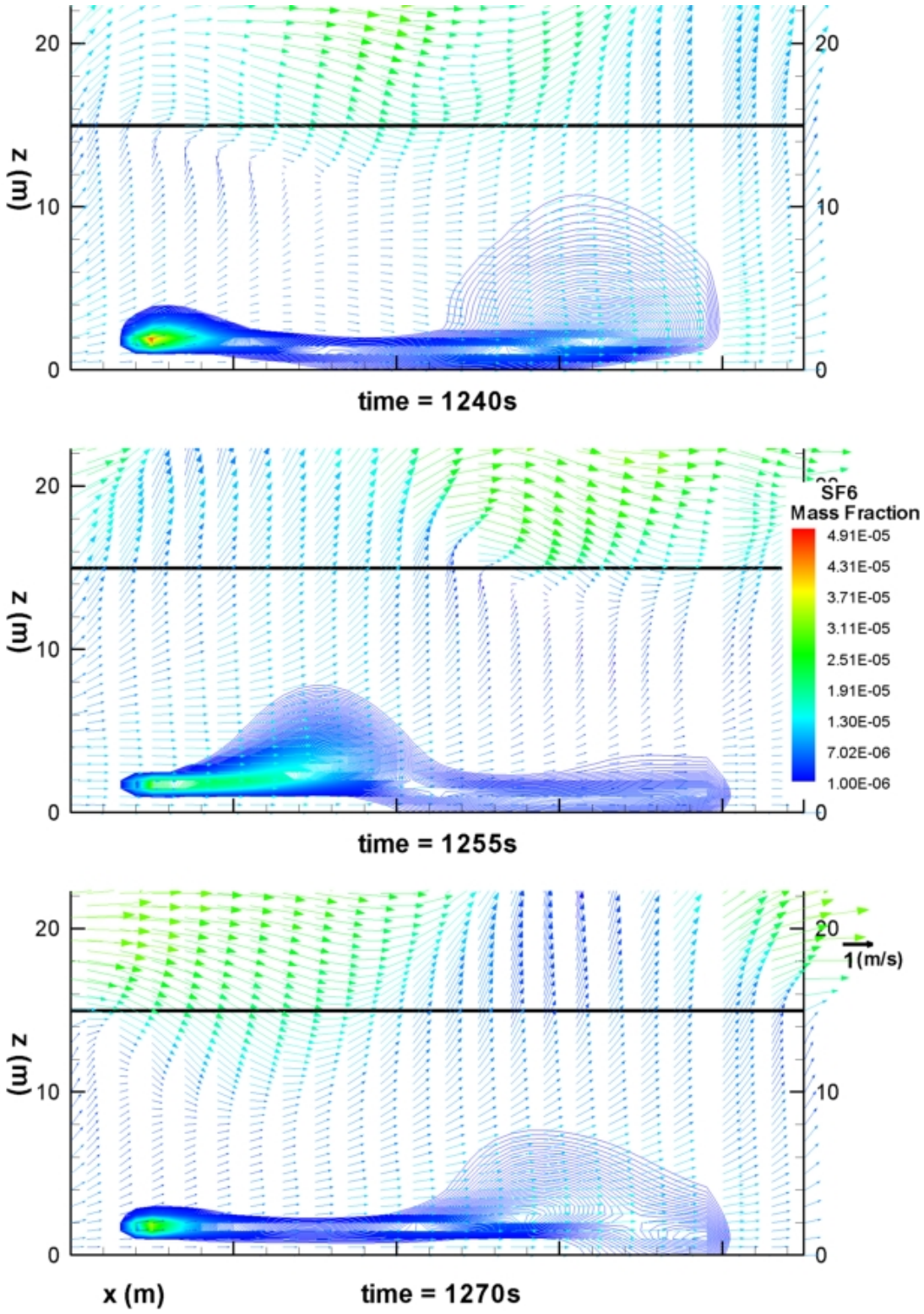


**Figure 29: Contours of $SF_6$ mass fraction overlaid on velocity vectors located on a vertical plane located at y = 15 m from a convective condition LES.**

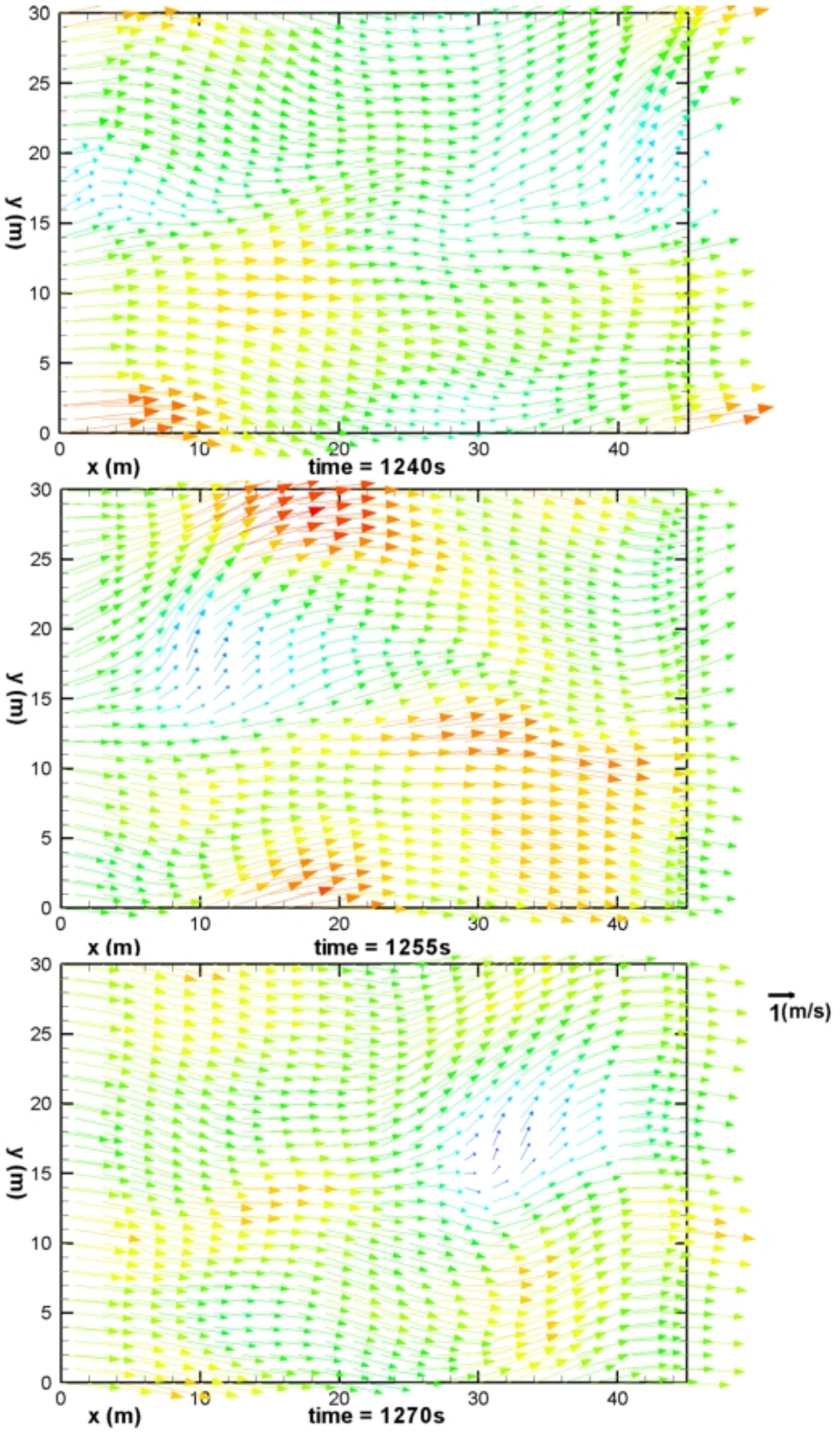


**Figure 30: Velocity vectors located on a horizontal plane located at z = 25 m from a convective condition LES.**

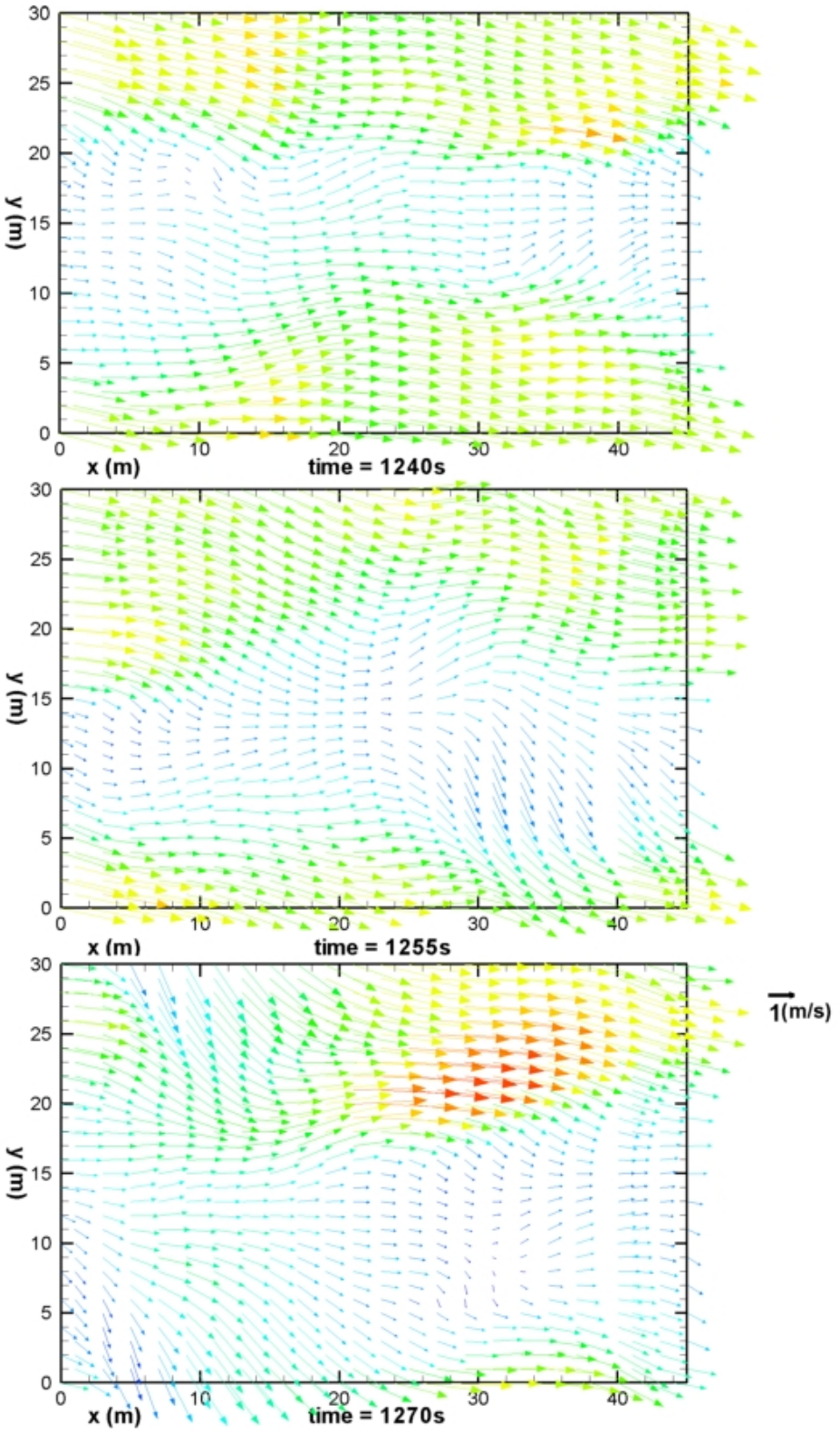


**Figure 31: Velocity vectors located on a horizontal plane located at z = 15 m from a convective condition LES.**

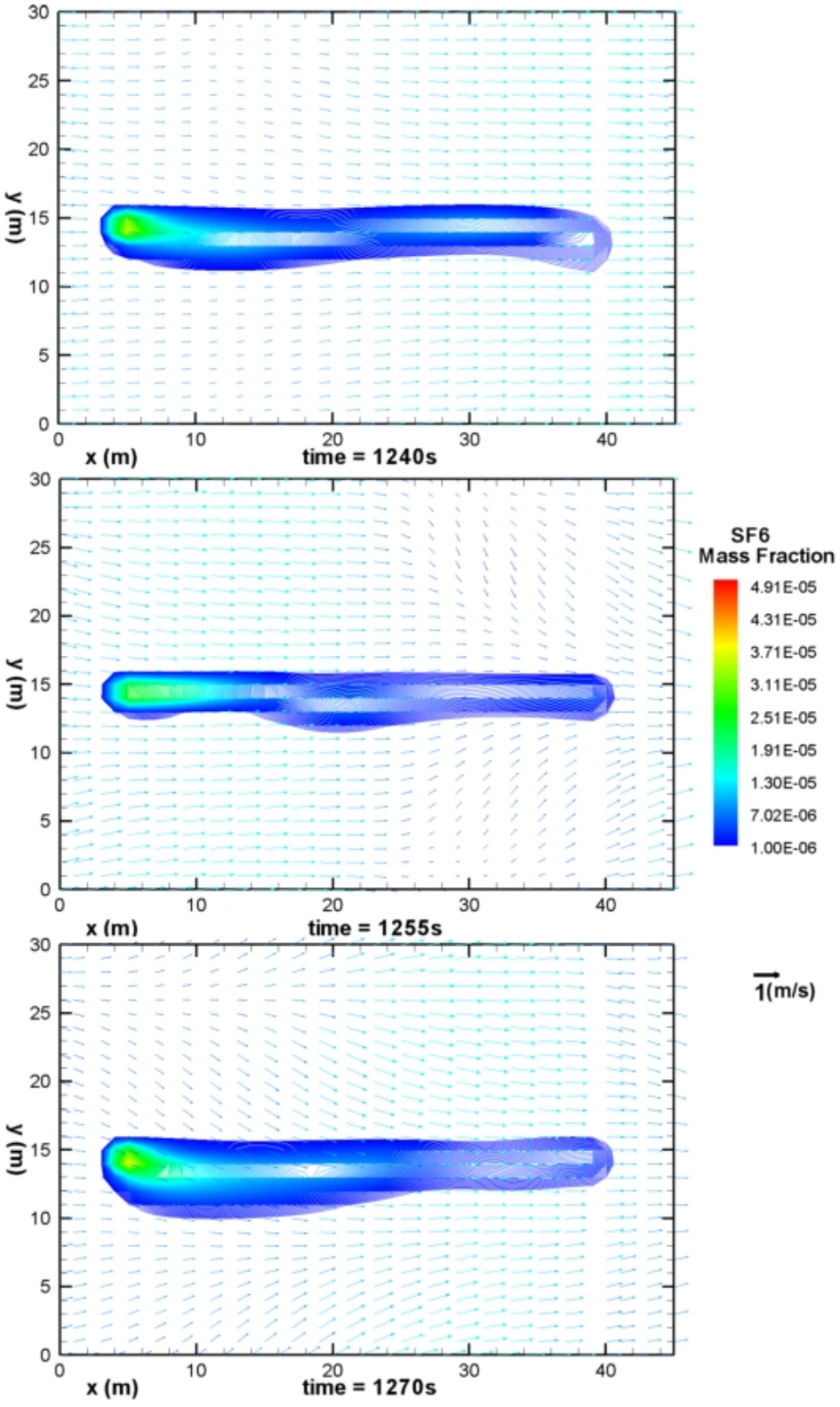


**Figure 32: Contours of $SF_6$ mass fraction overlaid on velocity vectors located on a horizontal plane located at z = 1.5 m from a convective condition LES.**

Contours of potential temperature on a vertical plane located at y = 15m are shown in Figure 33, and on a horizontal plane located at z = 15 m in Figure 34. Potential temperature is shown to be dynamic within and above the canopy by these two figures. A direct comparison can be made between Figure 33 and Figure 29 which shows that the buoyancy force produced by the potential temperature increases the vertical movement of the plume. Non-uniform potential temperature gradients are not predicted in the region close to the ground ($0 < z < h/3$). One would expect non-uniform potential temperature gradients to exist close to the ground in forest canopies and influence the buoyancy of a scalar. These non-uniform potential temperature gradients are generated by heterogeneous ground heat fluxes. A heat flux prescribed on the lower boundary condition is required to reproduce this physical phenomenon with LES. However, surface heat fluxes were not included in this preliminary investigation of LES. Thus an isothermal boundary condition was prescribed at the lower boundary condition, rather than applying an ad-hoc heat flux boundary condition.

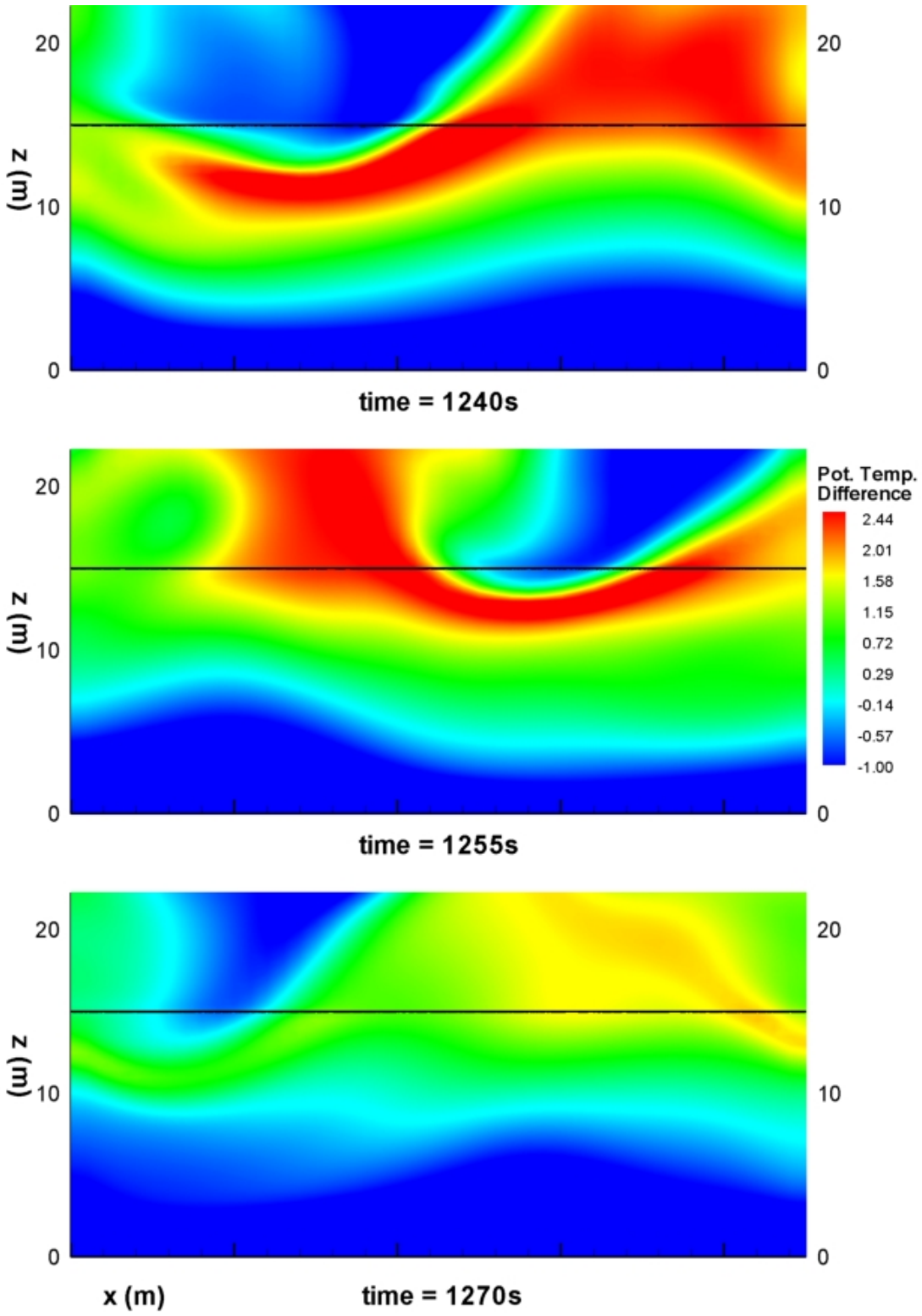


**Figure 33: Contours of potential temperature difference (θ- θ(h), θ (h) = 28 °C) located on a vertical plane located at y = 15 m from a convective condition LES.**

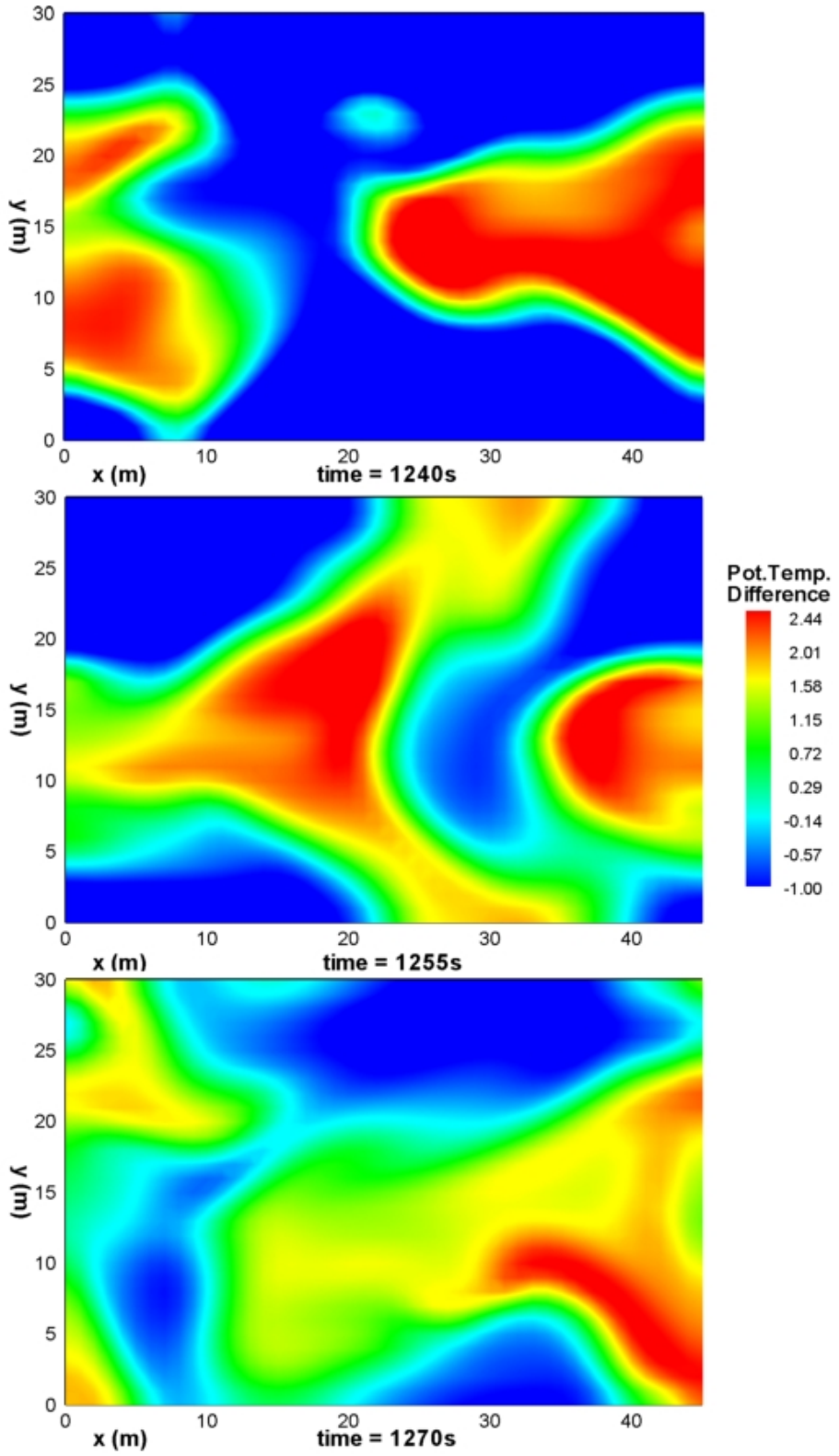


**Figure 34: Contours potential temperature difference (θ- θ(h), θ (h) = 28 °C) located on a horizontal plane located at z = 1.5 m from a convective condition LES.**

Instantaneous velocity signals corresponding to single computational cell are shown in Figure 35 and Figure 36. The magnitude of the velocity fluctuations are on the same order as observations from a smoothed sonic anemometer signal. Quadrant analysis of the velocity signal from a cell located at the canopy height (z = 15 m) and above the canopy (z = 25 m) are shown in Figure 25 and Figure 38 respectively. Both figures show evidence of bursting and sweeping. Furthermore, the magnitude of the bursting and sweeping are greater than the neutral stability case (Figure 25 and Figure 24). Intermittent plume movement is also shown in an instantaneous concentration of $SF_6$ time series (Figure 39). The computational cell output of $SF_6$ concentration exhibits behavior similar to measurements from a continuous analyzer. Figure 40 shows 5 minute average vertical $SF_6$ concentrations compared to observations. The predicted concentration from the convective LES case is approximately one and a half orders of magnitude greater than observations at 1.5 m above the ground. This discrepancy may be due to higher predicted velocities within the canopy, and the neglected ground heat source term.

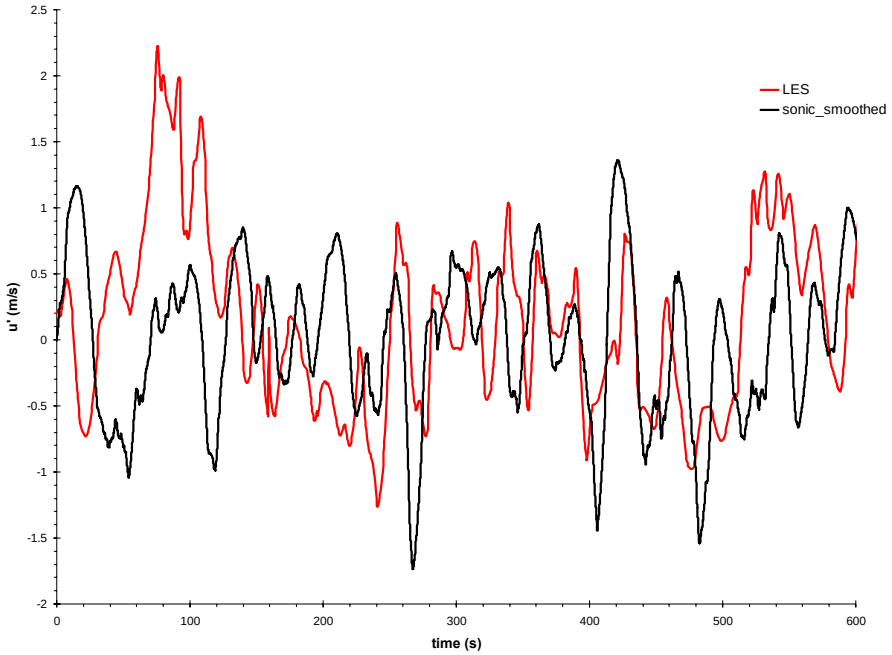


**Figure 35: Fluctuating stream-wise velocities from an averaged sonic signal, and LES output located at the canopy height z = 15 m from a convective condition LES. (** $\overline{u'^2}_{smoothed} = 0.52$ **m/s,** $\overline{u'^2}_{LES} = 0.40$ **m/s)**

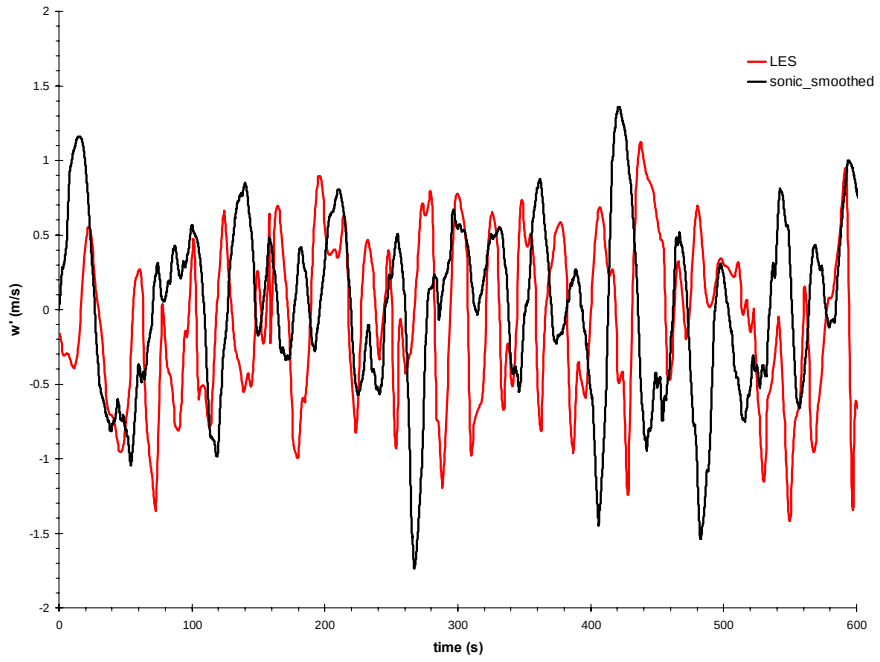


**Figure 36: Fluctuating vertical velocities from a sonic anemometer, an averaged sonic signal, and LES output located at the canopy height z =15 m from a convective condition LES.**
**(** $\overline{w'^2}_{smoothed} = 0.30$ **m/s,** $\overline{w'^2}_{LES} = 0.27$ **m/s)**

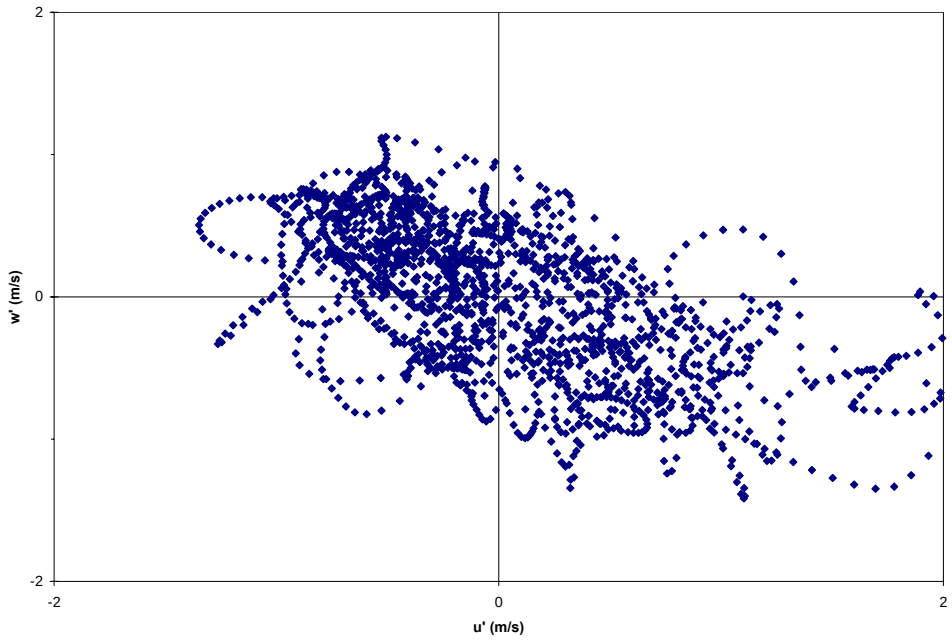


**Figure 37: Quadrant analysis from a cell located at z = h = 15 m from a convective condition LES.**

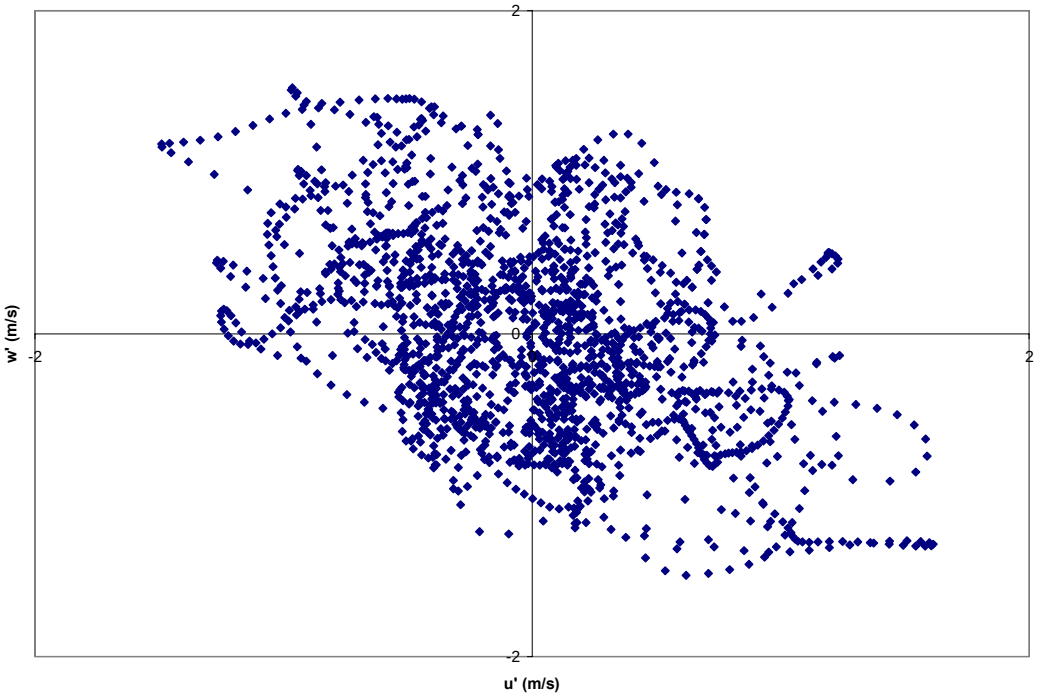


**Figure 38: Quadrant analysis from a cell located at z = 25 m from a convective condition LES.**

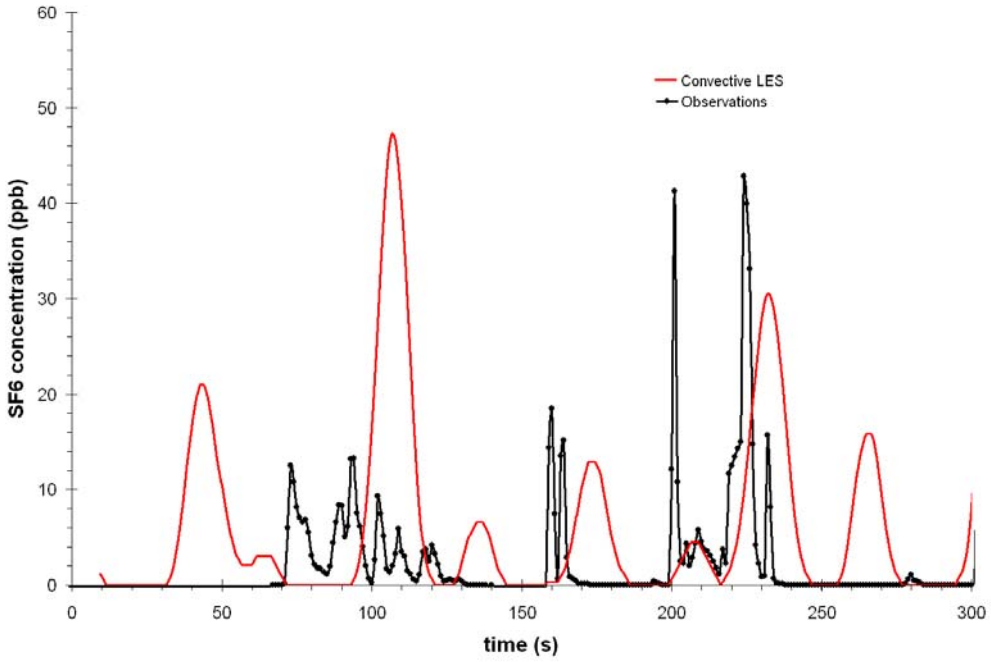


**Figure 39: Instantaneous concentration of $SF_6$ (ppb) from one computational cell output located 10 m from the release, from a convective condition LES. ($\overline{c'^2}_{obs} = 31.3$ ppb, $\overline{c'^2}_{LES} = 127.0$ ppb)**

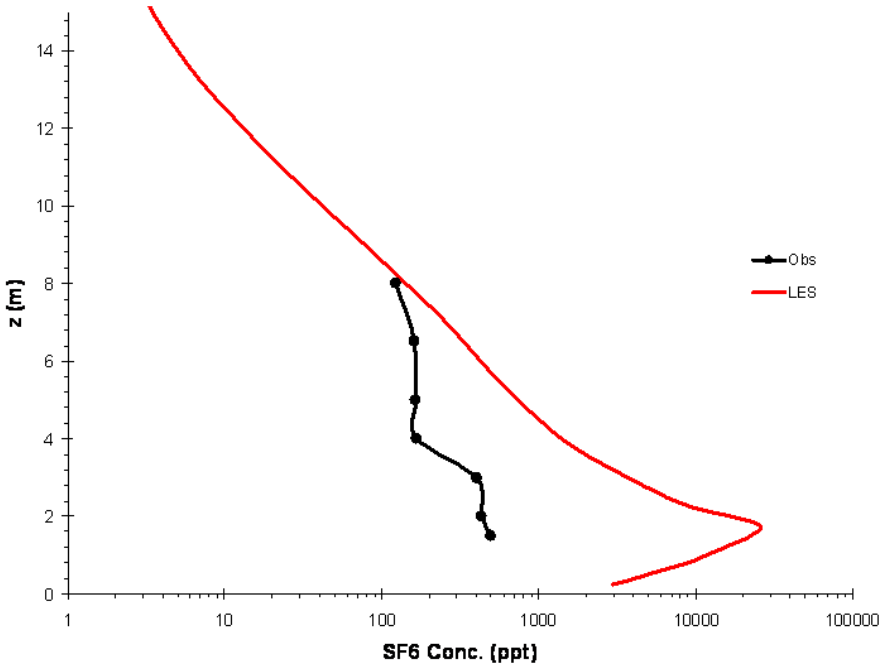


**Figure 40: 5min average vertical $SF_6$ concentration from a convective condition LES compared to field observations on May 25th 2005.**

Some remarks can be made by comparing results from the neutral LES case with the convective LES case. The mean stream-wise velocity is greater within the canopy ($0 < z < h$) in the convective case versus the neutral case. Vertical RMS velocity is higher in the convective case. The convective case shows enhanced vertical $SF_6$ transport and the fluctuating velocities are higher. These differences are expected due to the added buoyancy force generated by the solar heat source term.

LES-IQ was calculated for the computations by determining the amount of total and SGS kinetic energy. The LES-IQ was approximately 92% at the canopy height ($z = h = 15$m), and 95% above the canopy ($z = 25$ m) for the neutral case and 85% at the canopy height ($z = h = 15$ m), and 91% above the canopy ($z = 25$ m) for the convective case. According to Celik (2003) a LES solution has adequate cell resolution if the LES-IQ is greater that 75%. Thus, the LES computations are determined to have adequate cell resolution.

# CHAPTER 7: CONCLUSIONS

The objective of this research was to investigate the use of LES to simulate pheromone dispersion within and above forest canopies. The main mechanism for scalar transport within and above forest canopies is coherent motion. Coherent structures are driven by shear above the canopy and the buoyancy caused by solar heating within the canopy. In order for a model to accurately predict the transport of a pheromone within a forest canopy it must be able to simulate these coherent structures by capturing the instantaneous dynamics. The presented LES model captured the dynamics above and within a Loblolly forest canopy, such as bursting and sweeping. Thus, it appears that it is feasible to use LES to simulate tracer gas dispersion within and above a forest canopy.

Mean stream-wise velocity did not agree one to one with observations. This was expected due to the sparseness of the field data, and the uncertainty in the canopy drag and heat source parameterizations. A sensitivity analysis of the model may provide further insight into the factors that cause disagreement between mean simulated and observed stream wise velocity. However, conducting sensitivity analyses for LES runs is not presently feasible due to the computational cost of each simulation. Thus, the approach taken throughout this research was to report comparisons between general numerical simulations and experimental observations without modifying parameters between simulations. Recommendations for future experimental studies can be made based on this numerical study. Observations of temperature and heat flux close to the ground, temperature profiles throughout the canopy, surface roughness, and detailed LAD maps would be beneficial for model development.

More work is needed to understand the effects of changing the SGS model, domain size, grid resolution, canopy representation, solar heating parameterization, and complex terrain representation. Furthermore, plant canopy chemistry can be added to the model and the feasibility of conducting a reacting flow case could be investigated.

While conducting CFD simulations, specifically LES, a few important lessons were learned and are listed below.

1. Try to start with a simple test case whenever possible. This means a relatively low computationally expensive grid. One of the biggest drawbacks to CFD is the computational requirements, and amount of time it takes to produce solutions. It is not feasible to perform a sensitivity analysis on a large computation grid, therefore simple grids should be used for sensitivity analysis. Long turn around times are by far the biggest problem when learning a complex CFD program.
2. Keep a detailed record of all simulations. It seems obvious that one would remember parameters changed from simulation to simulation, or be able to open an old case file and determine what was done. This is not the case with CFD which produces hundreds of case files through the course of a research project. It is not feasible to go back through each file to determine which parameters were modified and why. Along with this should be a straight forward directory and naming system with both 'readme' files and records in the notebook.
3. Be patient. It is the nature of complex CFD to have long computation times. One must pick values to monitor, and allow a simulation to run it coarse until it is obvious the computation is diverging or is unstable. I was caught be surprise when I determined the computational time required for simple channel flow.

## REFERENCES


Amiro, B. D. (1990). "Drag coefficients and turbulence spectra within three boreal forest canopies." Boundary-Layer Meteorology **52**: 227-246.

Baldocchi, D. D. and T. P. Meyers (1988a). "A spectral and lag-correlation analysis of turbulence in a deciduous forest canopy." Boundary-Layer Meteorology **43**: 31-58.

Baldocchi, D. D. and T. P. Meyers (1988b). "Turbulence structure in a deciduous forest." Boundary-Layer Meteorology **43**: 345-364.

Bernard, P. S. and J. M. Wallace (2002). Turbulent Flow: Analysis, Measurement, and Prediction. Hoboken, New Jersey, John Wiley & Sons, Inc.

Celik I.B., N. Zeynep, et al. (2003) "Index of Quality for Large Eddy Simulation." Proceedings of the Forum on Turbulent Flow 2003 ASME Fluids Engineering Division Summer Meeting, Honolulu HI.

Dawson, P. J. (1987). A Numerical Model to Simulate the Atmospheric Transport and Diffusion of Pollutants over Complex Terrain. Department of Mechanical and Materials Engineering. Pullman, Washington State University**:** 194.

Denmead, O. T. and E. F. Bradley (1987). "On scalar transport in plant canopies." Irrigation Science **8**: 131-149.

Finnigan, J. (1979). "Turbulence in Waving Wheat II. Structure of Momentum Transfer." Boundary-Layer Meteorology **116**(213-236).

Finnigan, J. (2000). "Turbulence in Plant Canopies." Annual Review of Fluid Mechanics **32**: 519-571.

Gardiner, B. A. (1994). "Wind and wind forces in a plantation spruce forest." Boundary-Layer Meteorology **67**: 161-186.

Gullbrand, J. and F. K. Chow (2002). "Investigation of numerical errors, subfilter-scale models, and subgrid-scale models in turbulent channel flow simulations." Center for Turbulence Research, Proceedings of the Summer Program 2002.

Kaimal, J. C. and J. J. Finnigan (1994). Atmospheric Boundary Layer Flows: Their Structure and Measurement. New York, Oxford University Press.

Kim, J., P. Moin, et al. (1987). "Turbulence statistics in fully developed channel flow at low Reynolds number." Journal of Fluid Mechanics **177**: 133-166.

Kim, S.-E. (2004). "Large Eddy Simulation Using Unstructured Meshes and Dynamic Subgrid-Scale Turbulence Models." 34th AIAA Fluid Dynamics Conference and Exhibit.

Kline, S. J., W. C. Reynolds, et al. (1967). "The structure of turbulent boundary layers." Journal of Fluid Mechanics **30**: 741-773.

Leclerc, M. Y., K. C. Beissner, et al. (1990). "The influence of atmospheric stability on the budgets of the Reynolds stress and turbulent kinetic energy within and above a deciduous forest." Journal of Applied Meteorology **29**: 916-933.

Leclerc, M. Y., S. H. Shen, et al. (1997). "Observations and large-eddy simulation modeling of footprints in the lower convective boundary layer." Journal of Geophysical Research-Atmospheres **102**(D8): 9323-9334.

Patton, E. G., K. J. Davis, et al. (2001). "Decaying scalars emitted by a forest canopy: A numerical study." Boundary-Layer Meteorology **100**(1): 91-129.

Patton, E. G., P. P. Sullivan, et al. (2003). "The influence of a forest canopy on top-down and bottom-up diffusion in the planetary boundary layer." Quarterly Journal of the Royal Meteorological Society **129**(590): 1415-1434.
Raupach, M. R., R. A. Antonia, et al. (1991). "Rough-wall turbulent boundary layers." Appl. Mech. Rev. **44**: 1-25.
Raupach, M. R., J. J. Finnigan, et al. (1996). "Coherent eddies and turbulence in vegetation canopies: the mixing layer analogy." Boundary-Layer Meteorology **78**: 351-382.
Raupach, M. R. and A. S. Thom (1981). "Turbulence in and Above Plant Canopies." Annual Review of Fluid Mechanics **13**: 97-129.
Seinfeld, J. H. and S. N. Pandis (1998). Atmospheric Chemsitry and Physics: From Air Pollution to Climate Change. New York, John Wiley & Sons, Inc.
Shaw, R. H. and E. G. Patton (2003). "Canopy element influences on resolved- and subgrid-scale energy within a large-eddy simulation." Agricultural and Forest Meteorology **115**(1-2): 5-17.
Shaw, R. H. and U. Schumann (1992). "Large-Eddy Simulation of Turbulent-Flow above and within a Forest." Boundary-Layer Meteorology **61**(1-2): 47-64.
Shen, S. and Leclerc, M. Y. (1997). "Modelling the turbulence structure in the canopy layer." Agriculture and Forest Meteorology **87**: 3-25.
Su, H. B., R. H. Shaw, et al. (1998). "Turbulent statistics of neutrally stratified flow within and above a sparse forest from large-eddy simulation and field observations." Boundary-Layer Meteorology **88**(3): 363-397.
Thistle, H. W., H. Peterson, et al. (2004). "Surrogate pheromone plumes in three forest trunk spaces: Composite statistics and case studies." Forest Science **50**(5): 610-625.
U.S.D.A. Forest Service (2003). America's Forests Health Update. Washinton, D.C., U.S.D.A. Forest Service, Forest Health Protection**:** 14,15.
Versteeg, H. K. and W. Malalasekera (1995). An introduction to Computational Fluid Dynamics: The Finite Volume Method. Harlow, England, Prentice Hall.
Wallace, J. M., H. Eckelmann, et al. (1972). "The wall region in turbulent shear flow." Journal of Fluid Mechanics **54**: 39-48.
White, F. M. (1991). Viscous Fluid Flow, McGraw-Hill.
Willmarth, W. W. and S. S. Lu (1972). "Structure of Reynolds stress near the wall." Journal of Fluid Mechanics **55**: 65-92.

## APPENDEX A: Sample User Defined Function

```
#include "udf.h"

  FILE *ifpaa; /* instantaneous data at location aa = 2.5m */
   FILE *ifpbb; /* instantaneous data at location bb = 15m */
   FILE *ifpcc; /* instantaneous data at location cc = 25m */
   FILE *afpU; /* horizontal ave data for U */
   FILE *afpV; /* horizontal ave data for U */
   FILE *afpW; /* horizontal ave data for U */
   FILE *afpT; /* horizontal ave data for U */

DEFINE_EXECUTE_AT_END(average_execute_at_end)
{
   Domain *d; /* declare domain pointer since it is not passed as an
                 argument to the DEFINE macro  */

   real volume,vol_tot,vel,uavg,xx,y,z;
   real U,V,W,T,time;
   real U_ave_25m,V_ave_25m,W_ave_25m,T_ave_25m;
   real U_ave_20m,V_ave_20m,W_ave_20m,T_ave_20m;
   real U_ave_15m,V_ave_15m,W_ave_15m,T_ave_15m;
   real U_ave_10m,V_ave_10m,W_ave_10m,T_ave_10m;
   real U_ave_5m,V_ave_5m,W_ave_5m,T_ave_5m;
   real U_ave_2m,V_ave_2m,W_ave_2m,T_ave_2m;
   real x[ND_ND];
   Thread *t;
   cell_t c;
   d = Get_Domain(1);    /* Get the mixture phase domain using Fluent utility */

   thread_loop_c(t,d) /* Loop over all cell threads in the domain */
     {

     begin_c_loop(c,t) /* Loop over all cells  */
       {
       C_CENTROID(x,c,t);
          xx = x[0];
          y = x[1];
          z = x[2];
       U = C_U(c,t);
          V = C_V(c,t);
          W = C_W(c,t);
/*        T = C_T(c,t); */
       time = CURRENT_TIME;
          volume = C_VOLUME(c,t);   /* get cell volume */
```

```
/* write instantaneous values to file for position aa 8m*/

          if(z < 8.5){
        if(z > 8.0){
         if(y < 16.0){
          if(y > 14.5){
           if(xx < 11.5){
            if(xx > 10.0){

                    ifpaa =
fopen("c:/Fluent.Inc/work/channel/coarse/ke_soln/case_c/instant_aa.txt","a");
              fprintf(ifpaa,"%f %f %f %f \n",time,U,V,W);
                    fclose(ifpaa);



                          }
                         }
                        }
                    }
                   }
                  }

/* write instantaneous values to file for position bb 15m */

          if(z < 15.0){
        if(z > 14.5){
         if(y < 16.0){
          if(y > 14.5){
           if(xx < 11.5){
            if(xx > 10.0){

                    ifpbb =
fopen("c:/Fluent.Inc/work/channel/coarse/ke_soln/case_c/instant_bb.txt","a");
              fprintf(ifpbb,"%f %f %f %f \n",time,U,V,W);
                    fclose(ifpbb);

                          }
                         }
                        }
                    }
                   }
                  }
```

```
/* write instantaneous values to file for position cc 25m */

          if(z < 25.0){
        if(z > 24.0){
         if(y < 16.0){
          if(y > 14.5){
           if(xx < 11.5){
            if(xx > 10.0){

                    ifpcc =
fopen("c:/Fluent.Inc/work/channel/coarse/ke_soln/case_c/instant_cc.txt","a");
              fprintf(ifpcc,"%f %f %f %f \n",time,U,V,W);
                    fclose(ifpcc);

                                }
                               }
                              }
                            }
                           }
                          }
     }
    end_c_loop(c,t)

  }

}


DEFINE_INIT(my_init_function, domain)
{
 cell_t c;
 Thread *t;
 real x[ND_ND];
 real z, velocity, eps, k;

      thread_loop_c (t,domain)
   {

    begin_c_loop_all(c,t)
      {
        C_CENTROID(x,c,t);
        z = x[2];


        velocity = 0.2618*pow(z,0.6531);
```

```
        C_U(c,t) = velocity;

        C_K(c,t) = (-0.0015*z + 1.8095);

      if(z <= 1062.0)
            eps = (7.0*exp(8))*pow(z,-6.2362);
      if(z <= 53.0)
            eps = (-0.00012*z + 0.02);

      C_D(c,t) = eps;

      }
    end_c_loop_all(c,t)

  }
}


DEFINE_PROFILE(u, t, i)
{
 cell_t c;
 real x[ND_ND];
 real z,velocity;

 begin_c_loop (c,t)
  {


    C_CENTROID(x,c,t);
    z =x[2];


        if(z < 150.0)
            velocity = (3.34*(log((z))) - 8.73);
        if(z <= 15.0)
            velocity = 0.3;


    F_PROFILE(c,t,i) = velocity;
}
 end_c_loop (c,t)
}

DEFINE_PROFILE(e, t, i)
{
 cell_t c;
```

```
 real x[ND_ND];
 real z,eps;

 begin_c_loop (c,t)
   {


    C_CENTROID(x,c,t);
    z =x[2];

     if(z <= 1062.0)
            eps = (7.0*exp(8))*pow(z,-6.2362);
     if(z <= 53.0)
                 eps = (-0.00012*z + 0.02);


    F_PROFILE(c,t,i) = eps;
}
 end_c_loop (c,t)
}

DEFINE_PROFILE(k, t, i)
{
 cell_t c;
 real x[ND_ND];
 real z;

 begin_c_loop (c,t)
   {


    C_CENTROID(x,c,t);
    z =x[2];

    F_PROFILE(c,t,i) = (-0.0015*z + 1.8095);
   }
 end_c_loop (c,t)
}

DEFINE_PROFILE(porous_zone_z, t, i)
{
 cell_t c;
 real x[ND_ND];
 real z,p;

 begin_c_loop (c,t)
```

```
   {
/* centroid is defined to specify position dependent profiles*/

     C_CENTROID(x,c,t);
     z =x[2];

    if (z <= 500.0)
        p = 0.0;
    if (z <=15.0)
            p = 2*0.15*(-0.0074*pow(z,2) + 0.1372*z - 0.372) + (0.0342 - 0.00228*z);
    if (z <= 3.5)
            p = 0.0342;

            F_PROFILE(c,t,i) = p;


   }
  end_c_loop (c,t)
}

DEFINE_SOURCE(heat_source_lai, c, t, dS, eqn)
{

  real x[ND_ND];
  real con, source,z;


  C_CENTROID(x, c, t);
  z = x[2];

  if(z <= 500.0)
    con = 0.0;
  if (z <=15.0)
    con = -0.0006*(741*pow(z,2) - 13720*z + 3720)*exp(-0.001482*pow(z,3) +
0.04116*pow(z,2) - 0.02232*z - 0.9144);
  if (z <= 1.0)
    con = 0.0;

    source = con*C_VOLUME(c,t);
    dS[eqn] = 0;

  return source;
}

DEFINE_PROFILE(pot_temp, t, i)
{
```

```
  cell_t c;
  real x[ND_ND];
  real z,p;

  begin_c_loop (c,t)
    {
/* centroid is defined to specify position dependent profiles*/

     C_CENTROID(x,c,t);
     z =x[2];

    if (z <= 500.0)
        p = 292.366;
    if (z <=15.0)
           p = -.0576*z + 293.23;

           F_PROFILE(c,t,i) = p;


    }
  end_c_loop (c,t)
}

DEFINE_ADJUST(my_adjust, d)
{
  Thread *t;
  cell_t c;

  unsigned long idum1,idum2,idum3,idum;
  double fluct1,fluct2,fluct3;

  idum1 = 1;
  idum2 = 2;
  idum3 = 3;

  thread_loop_c (t,d)
  {
   begin_c_loop (c,t)

    idum1 = 1664525L*idum1 + 1013904223L;
    idum2 = 1664525L*idum2 + 1013904223L;
    idum3 = 1664525L*idum3 + 1013904223L;

    fluct1 = idum1/(4294967296.)-0.5;
    fluct2 = idum2/(4294967296.)-0.5;
    fluct3 = idum3/(4294967296.)-0.5;
```

```
      C_U(c,t)= C_U(c,t) + C_U(c,t)*0.25*fluct1;
      C_V(c,t)= C_V(c,t) + C_U(c,t)*0.25*fluct2;
      C_W(c,t)= C_W(c,t) + C_U(c,t)*0.25*fluct3;


   end_c_loop (c,t)
  }

}
```